

**UNCLASSIFIED**



**Australian Government**

**Department of Defence**  
Science and Technology

# The Whipping Response of a Submerged Platform Subjected to Near-field, Non-Contact Underwater Explosions

*Steven De Candia<sup>1</sup>, Roberto Ojeda<sup>1</sup>, Warren Reid<sup>2</sup> and Max Ratcliffe<sup>3</sup>*

**<sup>1</sup>Australian Maritime College  
University of Tasmania**

**<sup>2</sup>Maritime Division  
Defence Science and Technology Group**

**<sup>3</sup>Babcock Australasia**

**DST-Group-RR-0451**

## **ABSTRACT**

An experimental investigation of an underwater explosion (UNDEX) induced whipping response was conducted on a submerged platform. The platform was subjected to eight near-field, non-contact UNDEX events, using two explosive charge sizes at three longitudinal positions along the hull length, coinciding with predetermined peak and node positions of the natural bending mode responses of the platform. We found that stand-off positions at amidships, coinciding with the peak response of the first bending mode, produced the most severe whipping response. Stand-off positions located at the node of the first bending mode had a greatly reduced whipping response for the same charge size and transverse stand-off distance. Stand-off positions away from amidships demonstrated multiple bending mode responses, which for the larger charge size resulted in the peak response occurring away from the initial stand-off position. These results have an implication on how navy platform assessments are undertaken, and suggests that whipping responses require more detailed consideration to understand a platform's limitations against an UNDEX event.

## **RELEASE LIMITATION**

*Approved for public release.*

**UNCLASSIFIED**

UNCLASSIFIED

*Produced by*

*Maritime Division  
506 Lorimer Street  
Fishermans Bend VIC 3207*

*Telephone: 1300 333 362*

*Copyright Commonwealth of Australia 2018  
September 2018  
AR-017-282*

***APPROVED FOR PUBLIC RELEASE***

UNCLASSIFIED

**UNCLASSIFIED**

# The Whipping Response of a Submerged Platform Subjected to Near-field, Non-contact Underwater Explosions

## **Executive Summary**

An underwater explosion poses a significant threat to navy platforms. Understanding the performance of platforms against underwater explosions means designers and operators are aware of the requirements that need to be met for survivability and the limitations of the platform. To explore the responses that a submerged platform may undergo from an underwater explosion, a series of experimental tests were performed on a submerged generic cylindrical structure, approximately 12 m long and 0.4 m in diameter. A total of eight tests were performed using two Pentolite charge masses of 250 g and 43 g at different stand-off distances and locations along the hull length. Each test investigated how the charge size and stand-off location would affect the whipping response of this submerged platform.

We found that stand-off locations at amidships produced the most severe whipping response for both charge sizes, where the whipping response was dominated by the first bending mode of the platform for these events. For events where the charge stand-off location was near the theoretical nodal response position of the first bending mode, the whipping response was substantially reduced to the point that the initial shock response was more severe for both charge sizes. For charge stand-off locations near the theoretical peak response of the second bending mode of the submerged platform, the whipping response consisted of a superimposed response of the first, second, and third bending modes of the submerged platform. While the overall peak response was lower for stand-off locations away from amidships, some locations along the hull experienced similar severity during the whipping response. Notably, the larger 250 g charge at a 2.8 m aft stand-off from amidships had its peak response at the forward end of the platform, i.e. the most severe response occurred at the opposite end of the platform to where the charge was detonated.

These outcomes highlight the need to assess the platform as a whole model in a whipping analysis, to ensure that the global platform response to underwater explosion events is properly characterised. Individual compartment models are insufficient to capture these results. The results of these experiments will be used to validate numerical modelling procedures for underwater explosion induced whipping analysis of submerged platforms.

**UNCLASSIFIED**

UNCLASSIFIED

*This page is intentionally blank*

UNCLASSIFIED

## Authors

### **Steven De Candia**

Australian Maritime College

Steven De Candia graduated Bachelor of Engineering (Mechanical) from RMIT in 2015 and has since been undertaking a PhD in Maritime Engineering through the Australian Maritime College in partnership with DST Group and Babcock Australasia. Steven's work has focused on using Finite Element methods to analyse the response of naval platforms subjected to underwater explosions, most recently investigating the underwater explosion induced whipping response of submarine platforms.

---

### **Roberto Ojeda**

Australian Maritime College

Roberto Ojeda is the ship and offshore structures research leader at the National Centre for Maritime Engineering and Hydrodynamics of the Australian Maritime College, an Institute of the University of Tasmania. His research and teaching interests are in structural analysis and design of maritime structures with a special emphasis in survivability of naval platforms, ultimate strength, fluid structure interactions and crashworthiness of underwater vehicles.

---

### **Warren Reid**

Maritime Division

Warren Reid graduated from the University of Melbourne in 1983 with a Bachelor of Science (Honours) and joined the DSTO (now DST Group) the same year. Since then he has been involved in numerous projects on the metallurgical effects of shock loading and dynamic fracture of metals, and was awarded a Master of Applied Science Degree in 1995. In 1993 he was attached to Naval Surface Weapons Centre, Carderock for 15 months working on the shock loading of naval ships. He is currently Group Leader of the Dynamic Military Loads STC, Maritime Division, which examines the effects of primary weapons attack on surface ships and submarines. He is a member of Materials Australia, Engineers Australia and is a Chartered Professional Engineer.

---

## **Max Ratcliffe**

Babcock Australasia

Max Ratcliffe is Chief Engineer within the Submarines Business Unit of at the Adelaide office of Babcock Australasia. He has 18 years' industrial experience in the defence and civil nuclear sectors, predominantly in the structural analysis domain. Max holds a PhD from Bristol University in the UK in Structural Dynamics, where he investigated the use of prototype vibration test data to update Finite Element Models. He has regularly presented work to internal and external stakeholders, as well as having published several journal and conference papers. Max is a member of Engineers Australia and is a Chartered Professional Engineer.

---

## Contents

<b>1. INTRODUCTION.....</b>	<b>1</b>
<b>1.1 The UNDEX Phenomenon .....</b>	<b>1</b>
<b>1.2 UNDEX induced whipping.....</b>	<b>5</b>
<b>2. EXPERIMENT DESIGN AND SETUP.....</b>	<b>8</b>
<b>2.1 Experiment design .....</b>	<b>8</b>
<b>2.2 Scenarios and aims .....</b>	<b>13</b>
<b>2.3 Measurement instrumentation.....</b>	<b>15</b>
<b>3. RESULTS AND DISCUSSION .....</b>	<b>18</b>
<b>3.1 Incident pressure.....</b>	<b>18</b>
3.1.1 Shock wave.....	19
3.1.2 Bubble response.....	21
3.1.3 Pressure impulse .....	24
<b>3.2 Structural response .....</b>	<b>26</b>
3.2.1 The effect of transverse stand-off distance .....	30
3.2.2 The effect of longitudinal stand-off position .....	33
<b>4. CONCLUSION .....</b>	<b>42</b>
<b>5. ACKNOWLEDGEMENTS .....</b>	<b>43</b>
<b>6. REFERENCES .....</b>	<b>43</b>
<b>APPENDIX A ADDITIONAL MEASUREMENT SYSTEMS .....</b>	<b>48</b>

UNCLASSIFIED

DST-Group-RR-0451

*This page is intentionally blank.*

UNCLASSIFIED

## Glossary

UNDEX	Underwater Explosion
BEM	Boundary Element Method
FSI	Fluid Structure Interaction
USA	Underwater Shock Analysis code
DAA	Doubly Asymptotic Approximation
DST Group	Defence Science and Technology Group
UETF	Underwater Explosion Test Facility
BM	Bending mode
SOP	Stand-off point
TSOP	Transverse stand-off point
LSOP	Longitudinal stand-off point
TOA	Time of Arrival
T	Bubble period (ms)
K	Bubble period coefficient ( $\text{s}\cdot\text{m}^{5/6}/\text{kg}^{1/3}$ )
W	Charge mass (kg)
D	Depth (m)
I	Pressure impulse (MPa.ms)
I <sub>s</sub>	Shock wave pressure impulse (MPa.ms)
I <sub>B</sub>	Bubble pressure impulse (MPa.ms)
I <sub>T</sub>	Total pressure impulse (MPa.ms)
P	Pressure (MPa)
t	Time (ms)
γ	Bubble proximity parameter
R	Stand-off distance (m)
A <sub>max</sub>	Maximum bubble radius (m)
J	Maximum bubble radius coefficient ( $\text{m}^{4/3}/\text{kg}^{1/3}$ )

UNCLASSIFIED

DST-Group-RR-0451

*This page is intentionally blank.*

UNCLASSIFIED

# 1 Introduction

Navy platforms are required to operate in comparatively high-risk areas compared to commercial maritime platforms, which presents a challenge in their design and assessment. A unique threat that navy platforms may be exposed to is a weaponised underwater explosion (UNDEX). The UNDEX is a complex dynamic loading event, and it is difficult to predict exactly how this loading will interact with the platform, and the severity of the platform's response. Therefore, it is important that accurate and efficient UNDEX loading and response assessment methods are available to the navy as the operators and regulators, and to designers, so that the safe operational limits against UNDEX threats can be determined. Likewise, it is important to validate these assessment methods to increase the confidence levels for both the designer and the operator. Unfortunately individual navies generally do not make the results of full scale shock tests on their platforms available in the public domain. Thus, validated data of analysis methods against real platforms is not readily available. The purpose of this report is to provide design details and results of a generic platform subjected to a series of UNDEX events, which can be used for future UNDEX modelling validation.

## 1.1. The UNDEX Phenomenon

The UNDEX phenomenon has been described in detail by Cole [1]. In summary, it consists of two distinct loading phenomena: a high frequency shock wave, produced by the detonation of explosive material; and a low frequency, pulsating bubble of the explosive gas by-product. The pulsation cycles of the gas bubble result from a dynamic pressure imbalance between the compressible explosive gasses inside the bubble, and the external hydrostatic pressure of the near-incompressible water. Continuation of the pressure imbalance results from a build-up of fluid mass as the bubble expands, causing over-expansion and rapid contraction once this mass is lost. Each stage of the UNDEX phenomenon can be described by the incident pressure experienced at a given stand-off distance  $R$  from an explosive charge mass  $W$ , as shown in Figure 1.

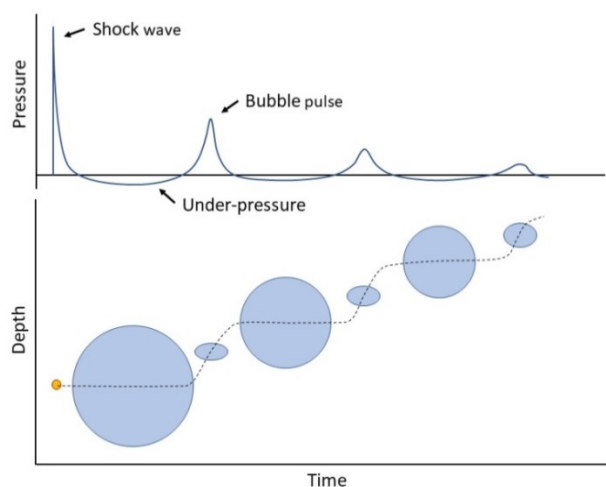


Figure 1: UNDEX event stages of the initial shock wave and migration of the pulsating bubble, with a characteristic incident pressure and pressure impulse experienced by a structure

The initial shock wave phase consists of a high pressure wave with a near instant rise time. The entire shock wave phase generally lasts no more than a few milliseconds. Initially the shock wave travels at the detonation velocity through the explosive material (approximately 6900 m/s for TNT [2]) until reaching the water boundary (the contact surface). The large difference in impedance across the contact surface causes the propagation velocity of the transmitted shock wave to rapidly reduce towards the acoustic wave velocity of water (approximately 1500 m/s). The reduction in velocity leads to a substantial increase in the pressure of the shock wave just beyond the contact surface, as per Bernouli's principle [1]. At a short distance beyond the contact surface, the temperature within the shockwave reduces to that of the surrounding ambient fluid and the energy of the shock wave is characterised by a stable combination of kinetic energy and volumetric strain energy of the hydrostatically compressed fluid medium, the later energy component being dominant. Under these conditions of a stable energy partition and near acoustic propagation (far-field shock wave conditions), peak pressure and pulse duration characteristics of the spherically spreading shock wave remain proportional with respect to charge mass  $W$  and stand-off distance  $R$  between the charge centre and Stand-Off Point (SOP). Based on observations of this similarity [1], empirical similitude equations from the parameter  $(W)^{1/3}/R$  have been developed to describe the primary characteristics of the shock wave.

Upon reflection of the compressive UNDEX shock wave from the water free-surface, a tensile relief wave of equal magnitude will propagate back towards the incident shock wave. The interaction of the tensile wave front with the tail of the incident shock wave can lead to a net pressure below the ambient hydrostatic pressure at a finite depth below the free-surface. Should the net pressure fall below the local vapour pressure of the water, a zone of cavitated water, known as a bulk cavitation [3], will form below the free-surface. The eventual collapse of the bulk cavitation zone, due to the weight of the water above the cavitation zone, may result in significant additional loading of nearby structures. Cavitation phenomena, referred to as hull cavitation, are also observed in the event of shock wave reflection from a flexible structural surface. Hull cavitation will occur if the relief wave generated by movement of the flexible surface in response to the incident shock wave is of sufficient magnitude to drive the local pressure (incident shock wave plus ambient hydrostatic pressure) to below the cavitation pressure. As in the case of bulk cavitation, collapse of the hull cavitation zone may result in significant additional loading of the adjacent structure.

The pulsating bubble phase lasts considerably longer than the shock wave, in the order of 100 to 1000 ms, depending on the explosive type, mass  $W$  and the charge detonation depth  $D$ . The incident pressure from the bubble shown in Figure 1, consists of long durations of negative gauge pressure due to the increasing fluid velocity as the bubble expands, referred to as the bubble under-pressure. This under-pressure is at its lowest when the bubble reaches its maximum radius. As the bubble collapses the incident pressure increases and immediately after this point of collapse a high-pressure pulse is emitted, referred to as the bubble pulse. Each pulsation of the bubble is considered as one bubble cycle (shock wave to first bubble pulse, first bubble pulse to second bubble pulse, etc.). The bubble pulsation period may be calculated from the similitude Equation 1.1 using an

empirical coefficient  $K$  from Swisdak [4] for the first bubble period, or from Swift and Decius [5] for up to three bubble periods, depending on the explosive material.

$$T = K (W)^{1/3} / (D + 10)^{5/6} \quad (1.1)$$

The peak pulse pressure produced at the bubble collapse is normally an order of magnitude lower than the peak pressure of the shock wave, but the durations of the pulse and the under-pressure loading are significantly longer. Therefore, the pressure impulse is often considered as a better representation of the effective dynamic loading contributions of the shock wave and bubble loads, as opposed to the peak pressure [6, 7]. A direct energy measurement of shock wave and bubble components is difficult to obtain in the underwater and explosion environments, but the pressure impulse is subjected to the same conservation laws as energy and therefore may be taken as a measurement of effective loading. The summation of the positive and negative pressure impulse magnitudes for the shock wave and the first bubble under-pressure yields the total impulse of the explosive at the measured stand-off distance  $R$ . The pressure impulse may be calculated directly from a pressure-time history  $P(t)$  using Equation 1.2.

$$I = \int_{t_0}^{t_1} P(t) dt \quad (1.2)$$

UNDEX events may be classified as occurring in either a near or far-field regime depending on the proximity of the bubble to a boundary [1]. For this report, a far-field event is defined as one where the bubble experiences no influence from a boundary. In contrast, a near-field event will consist of interactions between the fluid-flow field of the pulsating bubble and the reflective fluid-flow field from the boundary. These interactions appear as external forces on the bubble, known as Bjerknes forces [8]. Bjerknes forces may alter the bubble geometry and migration path depending on the boundary's geometry and material properties [9]. A dimensionless stand-off parameter  $\gamma$ , defined in Equation 1.3 as the ratio of the stand-off distance  $R$  to the maximum bubble radius  $A_{max}$  has been used by a number of authors [10-20] to describe the event regime and influence of the boundary on a near-field bubble response.  $A_{max}$  can be calculated using similitude Equation 1.4 with an empirical coefficient  $J$  from Swisdak [4].

$$\gamma = R / A_{max} \quad (1.3)$$

where

$$A_{max} = J (W)^{1/3} / (D + 10)^{1/3} \quad (1.4)$$

The generalised form of the stand-off parameter does not account for all variables of bubble-structure interaction, such as curvature and the degree of flexibility of the boundary, or the relative size of the bubble with respect to a finite boundary size. Due to these variables, there is currently no scientific consensus on an exact value of  $\gamma$  that may define the border between near or far-field regimes. For bubble models that utilise an ideal spherical assumption [21-23], a value of  $\gamma > 2$  is often considered as far-field. More detailed studies on the interaction of bubbles to rigid boundaries [10-14] have found that at values

of  $\gamma < 2$  the Bjerknes forces attracted the bubble to the boundary and reduced the bubble's pulsation period. An experimental investigation conducted by Zhang, et al. [14] showed that a bubble migrating vertically towards the free-surface would experience limited attraction to a perpendicularly suspended flat rigid boundary when  $\gamma = 1.4$ , though the bubble was still able to undergo a complete set of pulsation cycles and vertical migration without collapsing onto the boundary. In an additional experiment with a horizontal plate representing a rigid floor, parallel to the free surface, the Bjerknes forces were essentially balanced with the buoyancy forces on the bubble when  $\gamma = 1.2$ , which prevented any significant migration during the early pulsation cycles. An experimental study from Tomita, et al. [11] found that convex curvature of the boundary reduced the Bjerknes forces, while concave curvature increased them. It was also observed that the Bjerknes and buoyancy forces were in equilibrium when the bubble interacted with a solid sphere of similar radius when  $\gamma = 1.6$ . This arrangement prevented any bubble migration.

There are few studies on the effects of bubbles near flexible boundaries, and it is difficult to distinguish the amount of flexibility that influences the Bjerknes forces acting on the bubble. However, it is known that near a relatively flexible boundary the Bjerknes forces will repel the pulsating bubble and the pulsation period increases [14]. This effect is commonly observed when a bubble interacts with the free-surface [15, 16], and has also been explored in medical applications on tissue material analogues [17, 18]. These medical studies identified that the Young's modulus of the boundary material influenced the repulsive response. Gibson and Blake [24] conducted an experimental study on cavitation bubbles collapsing near a flexible rubber boundary and found that reduced stand-off distances and different rubber material thickness had negligible effect on the repulse bubble response. It was concluded from Gibson and Blake's study that the limiting values for the bubble inertia and boundary flexibility that induce the repulsive effect remain unknown.

In close proximity (as  $\gamma$  approaches 1.0), the bubble may collapse on the boundary [25]. In this case, a low pressure zone develops between the bubble and boundary. The bubble begins to flatten and the pressure difference on the boundary side and free side of the bubble cause the surrounding fluid to accelerate through the bubble, producing a toroidal form. The water accelerating through the bubble forms a distinct column, known as the bubble jet, that shoots towards the rigid boundaries and away from flexible ones [26]. For UNDEX weapon sized bubbles, the force from the bubble jet can be large enough to pierce through hull plate and multiple decks of a surface platform [27].

All these studies were conducted at substantially smaller scales than even a small UNDEX bubble, which raises the question of how these responses might be influenced by the relative scale of the bubble and boundary in a similar fluid. There is surprisingly very little information regarding how the relative size of the bubble to a boundary will affect the response of each, although three broad scenarios of interaction may be interpreted from the literature.

The first scenario considers a small bubble near a relatively infinite sized boundary. Here the bubble will itself deform but the boundary is unlikely to experience any significant motion because of the bubble interaction. Such a situation is often the focus of cavitation

bubble collapse studies [28-30]. In the context of an UNDEX, the shock wave loading would likely be the greater concern in this scenario.

The second scenario considers a large bubble against a relatively small boundary. Here the bubble will not experience any significant deformation itself or be influenced by any significant Bjerknes forces between itself and the boundary. The structure will likely experience a global motion response from the bubble. For example, Zhang, et al. [31] noted a spark generated bubble was relatively undisturbed by the presence of the small electric ignition probes used in their experiments, while the report of the Crossroads Baker underwater nuclear explosion test detailed how a ship momentarily floated atop the dome of the large bubble at the surface before disintegrating as it burst [32]. This scenario would be an unlikely assessment in the UNDEX context, as the loading from an UNDEX of this relative size would greatly exceed any reasonable design considerations.

The final scenario considers a bubble and control length of a boundary (e.g. a hull diameter) to be in the same order of size. Here it is suggested that the dynamics of both the platform and bubble are dependent on each other [11]. There is limited understanding on exactly what relative size limits apply to this interaction, other than that they are “comparable”. It is this coupled bubble-structure interaction scenario that is of interest to the experimental investigation discussed in this report. It is hypothesised that the coupled interaction could induce a more severe whipping response than what could be caused by just the shock wave and uncoupled bubble pulse loads from a far-field UNDEX event.

## 1.2. UNDEX induced whipping

UNDEX induced whipping is a global dynamic bending response of a platform due to the loading from the shock wave and successive bubble loading cycles from an UNDEX event [21]. These periodic loadings can excite modal responses in the structure, the most significant of these being the Bending Mode (BM) responses. Most maritime platforms take the generalised form of a free-free ended beam, and the first three BMs, illustrated in Figure 2 where  $j$  is the number of half sine waves, are considered as the most significant concern for UNDEX induced whipping [21].

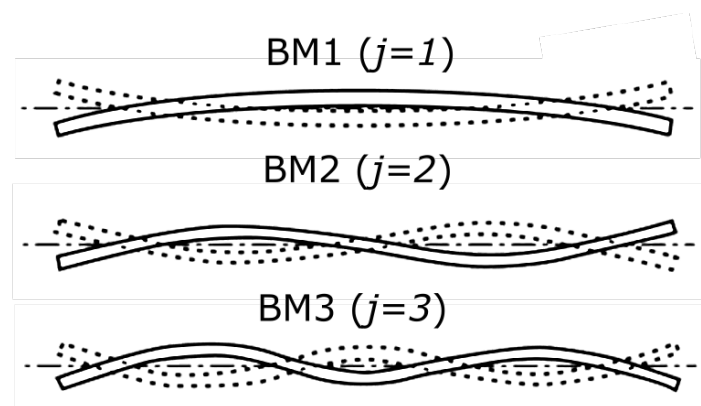


Figure 2: Bending mode shapes of a free-free uniform beam

In addition to BMs, a combination of circumferential and axial modes, noted in Figure 3 using the notation from Blevins [33], may also be excited in a submarines pressure hull.

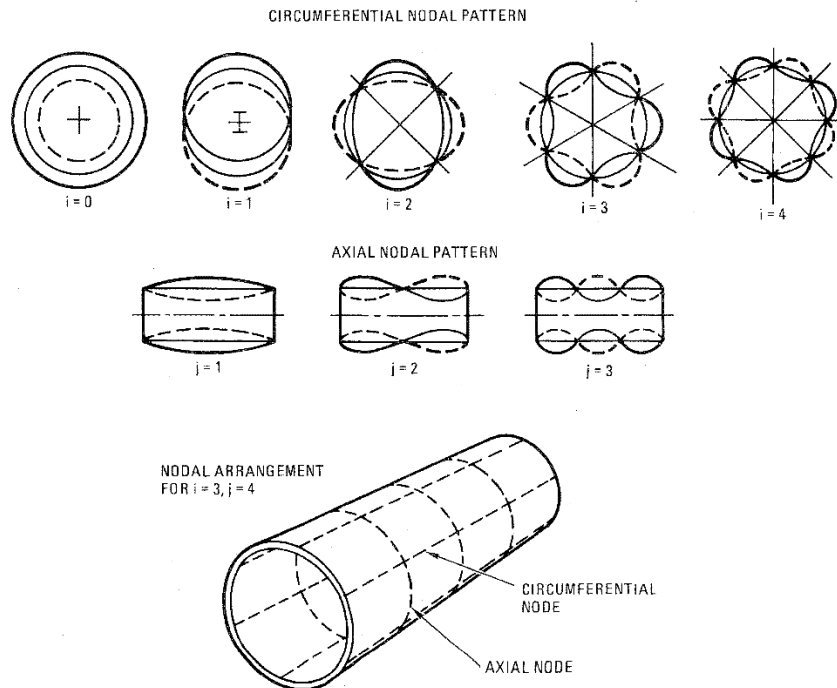


Figure 3: Circumferential and axial responses of a uniform free-free cylinder

The amplitude of these modal responses can potentially amplify over successive bubble cycles when the bubble loading frequency is near any of the modal response frequencies of the platform. For both submarine and surface platforms, a whipping response of high enough amplitude can result in the ultimate strength failure of longitudinal structural elements such as the keel or deck, and/or induce interframe or overall buckling collapse of the hull structure. In the case of submarine platforms, it is noted by Burcher and Rydill [34] that a whipping response is the most likely failure mode of the pressure hull, as the ring-stiffened pressure hull design is inherently susceptible to longitudinal strength failure at the stiffener hard-points from a global bending response.

A platform's UNDEX survivability is generally evaluated through a combination of empirical standards and analytical analysis. Empirical standards consider platform and equipment response under different shock classes [35]. These shock classes are determined from UNDEX experiments conducted on real world platforms [36] or model analogues that represent key features of platform structure [37]. De Candia, et al. [38] discussed a number of key experiments that have been published for benchmarking purposes and noted that few of them considered whipping responses in their assessment. Furthermore, the reported experiments offer limited data, with shock loading and response being the primary focus of these experiments. The shock class qualification method has an inherent limitation in that it is entirely based on previous design testing. This can make it difficult to apply to new platform designs and equipment systems, particularly if these deviate greatly from anything that was considered on the test platform. The use of an analytical assessment method allows designers to overcome this limitation.

Analysis of surface and submarine platform whipping responses was first considered by Chertock [39] who derived analytical solutions using a method of modal superposition of the structural response frequencies, based on the contributions from the pulsating bubble. Chertock's analytical solution was derived from a set of experiments conducted on small scale surface barge and a submerged ring-stiffened pressure hull models, to accommodate the use of 1.2 g TNT detonator charges [40]. It must be noted that Chertock's method was developed prior to the availability of the modern computer, and the simple models and experimental setup resulted in limitations to the method's applicability and accuracy. A review of whipping analysis techniques by Bannister [41] noted four major simplifications that were considered in the solution:

1. The structure was considered as a uniform section, and the mass distribution was idealised as uniform across the length of the structure. This is rarely the case for a real platform.
2. The method is based on modal superposition, so only linear responses can be considered.
3. The effects of bubble migration to the surface are neglected, so the bubble is assumed to be stationary in space.
4. A spherical bubble is assumed, so this method may only be accurate for a far-field UNDEX scenario.

While Chertock noted good correlation on the surface barge events, the analysis overpredicted the displacement of the submerged pressure hull model, due to the third bending mode response, by around 30% when charges were detonated away from amidships. The error was attributed to the non-uniform mass distribution in the experimental model.

With the increased availability of computing power, Hicks [21] was able to overcome most of the limitations from Chertock's method, using numerical analysis methods. Hicks applied a geometric transform based on the added mass expressions from Lewis [42] to account for the non-uniform mass distribution of a typical surface ship hull form. Hicks also developed a spherical migrating bubble model that accounted for the first bubble pulsation cycle. It was noted that due to the assumption of a spherical bubble, the model was only accurate for applications where the bubble is not distorted by the interaction with the vessel, which is considered applicable for only far-field UNDEX events.

Modern numerical analysis methods used to investigate UNDEX induced whipping mainly rely on a Boundary Element Method (BEM) or full Fluid-Structure Interaction (FSI) analysis techniques. A BEM analysis contains a full structural model but simplifies the representation of the fluid domain and boundary conditions. A common BEM tool is the Underwater Shock Analysis (USA) code [43]. This uses an iterative solution of the Doubly Asymptotic Approximation (DAA) from Geers [44] to model the high frequency and low frequency response asymptotes of a structure partially or fully immersed in fluid. Idealised shock and bubble models from Hicks [21] and Geers and Hunter [22, 23] may be used to initiate a loading source, or a user defined incident pressure and velocity may be specified. Like all other methods using idealised bubble models, accuracy of these loading models may be limited to far-field UNDEX events. The BEM is also limited by its ability to

accurately capture cavitation loading due to the fluid-structural boundary coinciding with the BEM interface.

A hybrid BEM-FSI analysis may be performed by the application of the BEM to a fluid mesh surrounding the structure to capture cavitation without the high computational cost of modelling the explosive detonation.

Full FSI analyses involve the physical modelling of structure, fluid and explosive domains. The small time-scale and high mesh fidelity needed for detonation and shock wave modelling, combined with the relatively long duration of the bubble pulsation cycles make this an intensive computational effort by any measure. However, this method is not limited by idealised bubble models, so a non-spherical bubble and effects due to the boundary interaction can be modelled [45, 46].

To better understand the FSI that occurs between near-field UNDEX and a platform, the effects of the bubble-structure coupling need to be explored, to determine how this may affect the severity of a whipping response. Analysis methods for UNDEX induced whipping responses also need to be validated to improve the design and qualification processes. The aim of this investigation is to provide the scientific community with a data set, for numerical analysis validation and for benchmarking studies of different numerical analysis methods. This paper discusses the methodology and the results from an experimental investigation aimed at characterising the whipping response of a submerged free-ended, hollow cylinder subjected to near-field, non-contact UNDEX events. This investigation explores the influence that different charge sizes, and transverse and longitudinal stand-off distances have on the whipping response of a fully submerged platform.

## 2 Experiment design and setup

### 2.1. Experiment design

The experiments were conducted at the Defence Science and Technology (DST) Group Underwater Explosion Test Facility (UETF) in Epping, Victoria. The facility is a flooded quarry with approximate dimensions of  $100 \times 40$  m, as shown in the overview in Figure 4, and water depth varying from 12 to 16 m. A nominal test depth of 5 m was specified to limit boundary interaction effects from the free surface and the quarry floor.

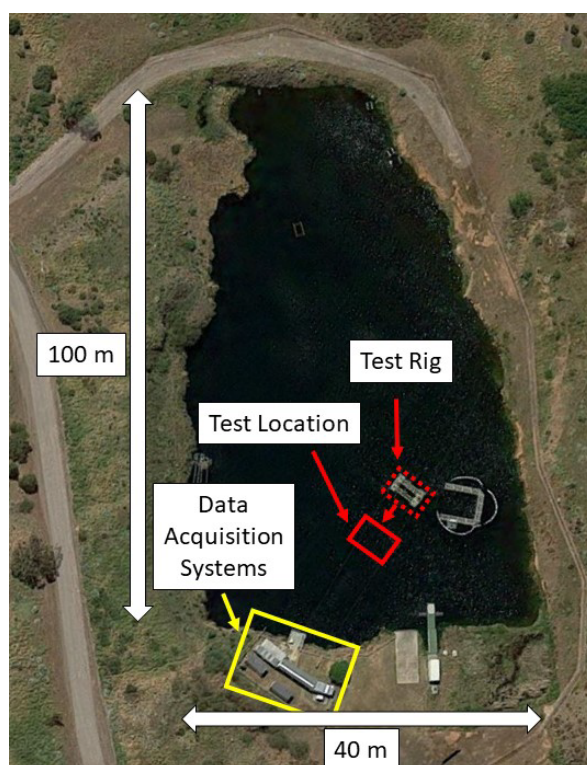


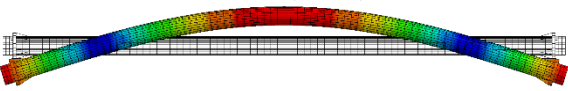
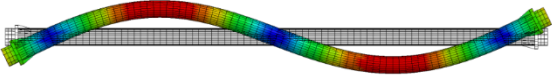
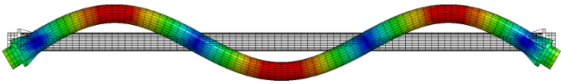
Figure 4: Overview of the DST UETF and test platform location

A design study for a free-free ended hollow cylindrical section beam structure (the platform) was conducted. The hull of the platform was constructed from a standard pipe size. It was determined that based on the test area size and depth, and the standard pipe sizes available, that a maximum charge size of 250 g of Pentolite could be used and not pose a significant risk of yielding the platform hull. The design of the platform hull was primarily based on achieving a similar natural bending mode response frequency to the frequency of bubble pulsations from the 250 g pentolite charge detonated at a depth of 5 m, which was calculated to be 7.2 Hz from Equation 1.1. From these design constraints, a 12 m long, 400 mm nominal diameter (DN400), 6.35 mm thick (SCH10) standard pipe was selected for the platform hull. The platform hull was manufactured from C350 grade cold rolled steel according to standard AS1163 [47]. The platform hull was fitted with flat flanges at each end and flat endcap seals, constructed according to standard AS2129 Table E [48]. Each endcap had a purpose-built rack mount system to attach disk weights, which were used to control the platform's net buoyancy and to tune its bending mode frequency response to the bubble frequency. The overall design and additional structural features are shown in Figure 5. Each disk weight was approximately 25 kg and the final configuration utilised nine disk weights at each end, for a total additional mass of 450 kg. This provided a reserve buoyancy of approximately 80 kg.

A wet modal analysis was performed on this early stage design of the platform to predict the bending mode response shapes and frequencies when the platform was fully submerged at a centreline depth of 5 m. This was achieved using the implicit LS-Dyna solver [49] coupled with the USA code [50], which calculates the added fluid mass using the boundary integral method described by Deruntz and Geers [51]. The platform was

expected to behave as a free-free ended beam, and therefore it was anticipated that the lowest Bending Mode (BM) responses would be dominant. The first three BM response shapes and frequencies are presented in Table 1, with longitudinal distances of the response shape peak and node positions measured from amidships. These shapes and locations were used to determine the explosive charge and instrumentation locations.

Table 1: Bending mode response frequencies and the longitudinal positions of the response shape peaks and nodes, relative to amidships

Bending Mode	Frequency	Peak positions (m)	Node positions (m)
<p><b>2-node (BM1)</b></p> 	6.8 Hz	0.00, ± 6.00	± 4.30
<p><b>3-node (BM2)</b></p> 	20.3 Hz	± 2.80	0.00, ± 5.25
<p><b>4-node (BM3)</b></p> 	41.6 Hz	0.00, ± 3.90	± 1.95, ± 5.62

Additional functional modifications were made to the early platform design. Three access portholes were constructed into cut-out sections that were welded back into the hull and reinforced to maintain the watertight integrity against UNDEX loading. These portholes were used to install and remove internal measurement transducers located at amidships and at 2.8 m forward and aft, as noted in Figure 5. A cable gland was inserted at the top of the pipe for running data cables to the on-shore data acquisition systems.

Six outriggers were used to suspend pressure gauges and position the explosive charge with respect to the hull. These were fixed by a clamped saddle design around the hull. The design also allowed these to be repositioned during the experiment.

The locations of the portholes and outriggers corresponded to the peak bending response locations of the BM1 and BM2 mode shapes, noted in Table 1. The total mass of the full platform outfit, including all modifications and measurement transducers, was measured as  $1548 \pm 1$  kg. A breakdown of the mass for major components, presented in Table 2, was calculated from CAD geometry and real measurements of the actual platform. An approximate mass distribution is shown in Figure 6.

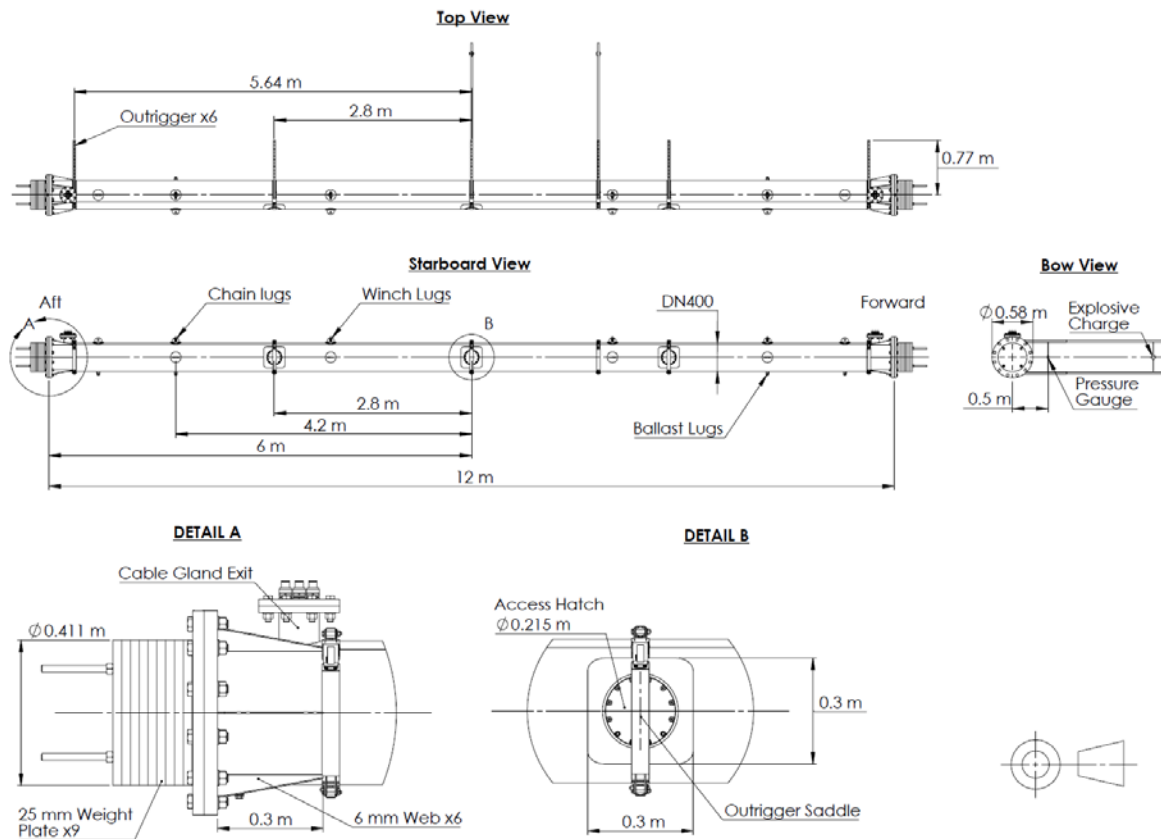


Figure 5: Schematic of the platform with detailed features of the end assembly and portholes

Table 2: General breakdown of the platform structure and component masses

Component	Mass (kg)	Quantity	Total (kg)
Pipe Hull	735	1	735
End Flanges	36	2	72
Endcaps	65	2	130
End Masses (per end)	25	18 (9)	450 (225)
Outriggers	7	6	42
Access port inserts	6	3	18
Sealing caps	5	3	15
Transducers, cables, fixtures and weldments	86	1	86
<b>Total</b>			<b>1548±1</b>

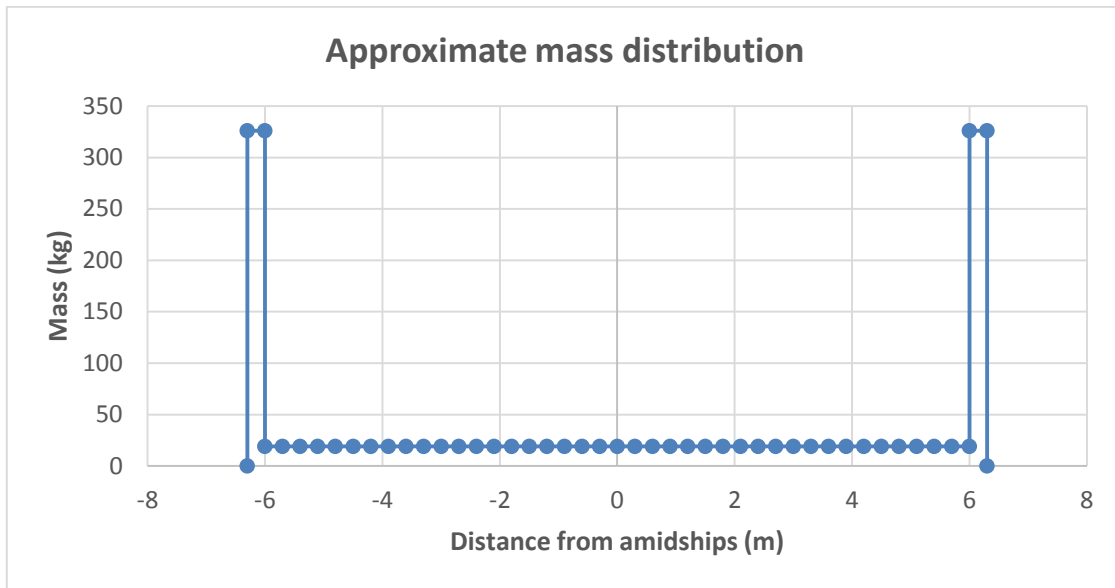


Figure 6: Approximate mass distribution of cylinder and end masses.

The platform was suspended from a floating test rig at a centreline depth of 5 m. A total of 100 kg of ballast mass was suspended by chains below the platform, split evenly between 4.2 m forward and aft of amidships as shown in Figure 7, to overcome the positive buoyancy. The location of the vertically suspended mass was at the expected nodal points of BM1 and thus it was judged that the mass would have negligible effect on the platform's horizontal response.

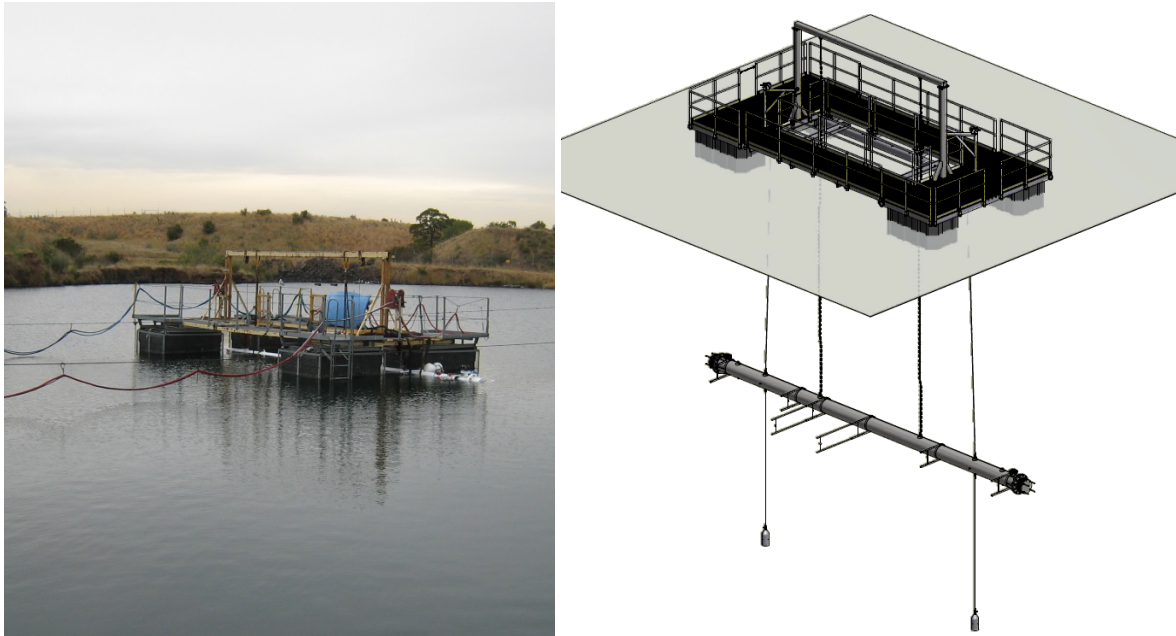


Figure 7: Floating test rig with platform suspended below

## 2.2. Scenarios and aims

Eight UNDEX events were performed on the platform using military grade Pentolite explosive charges. Each event considered the variables of the explosive charge mass  $W$ , and Stand-Off Point (SOP) in the Transverse (TSOP), and the Longitudinal (LSOP) directions. The TSOP is defined as the distance from the platform hull surface to the centre of the explosive charge. The LSOP is the distance from amidships to the centre of the explosive charge.

Two explosive charge sizes, 250 g and 43 g, were used in this set of experiments, both detonated at the same depth of 5 m. The variables of each charge size are presented in Table 3. The maximum bubble radius  $A_{max}$  was calculated from Equation 1.4 for each charge size, using coefficient  $J = 3.52$  from Table 10 of Swisdak [4]. The first  $T_1$  and second  $T_2$  bubble periods were calculated from Equation 1.1, using coefficient  $K = 2.11$  from Table 10 of Swisdak [4] for the first bubble period and  $K = 1.59$  for the second bubble period, based on an average value of the Pentolite data from Table XI of Swift and Decius [5]. It is worth noting that this Pentolite dataset for the second bubble cycle consists of only two results and the scenarios conducted in this experiment are outside the ranges of this dataset. Therefore, the predictions for the second bubble period may not be as accurate as those for the first bubble period. The pulsation frequency of the first  $f_1$  and second  $f_2$  bubble cycles was determined from the inverse of the period. The similar frequency of the 250 g bubble  $f_1$  and the BM1 response of the platform was expected to induce a strong whipping response, while the mismatched frequencies of the smaller 43 g charge bubble were expected to induce a weaker whipping response.

Table 3: Explosive charge bubble variables

<b>W</b> (g)	<b>A<sub>max</sub></b> (m)	<b>A<sub>max</sub>/R<sub>c</sub></b>	<b>T<sub>1</sub></b> (ms)	<b>T<sub>2</sub></b> (ms)	<b>f<sub>1</sub></b> (Hz)	<b>f<sub>2</sub></b> (Hz)
<b>250</b>	0.9	4.5	140	106	7.2	9.4
<b>43</b>	0.5	2.5	78	59	12.9	17.0

The UNDEX events were arranged as shown in Figure 8 with the variables detailed in Table 4. All events were detonated on the port side of the platform. The stand-off parameter  $\gamma$  was calculated from the TSOP and  $A_{max}$  using Equation 1.3, where  $TSOP = R$ . It is shown in Table 4 that  $2.00 \geq \gamma \geq 1.45$ , and the ratio of  $A_{max}$  to the hull radius  $R_c$  is in the same order of magnitude for all events. Given these conditions, it was expected that there would be a coupling of the bubble and platform responses, but sufficient distance to prevent direct collapse of the bubble on the platform. A placement tolerance for the LSOP and TSOP was defined as 0.04 m, accounting for a maximum misalignment of 10% relative to the platform hull diameter.

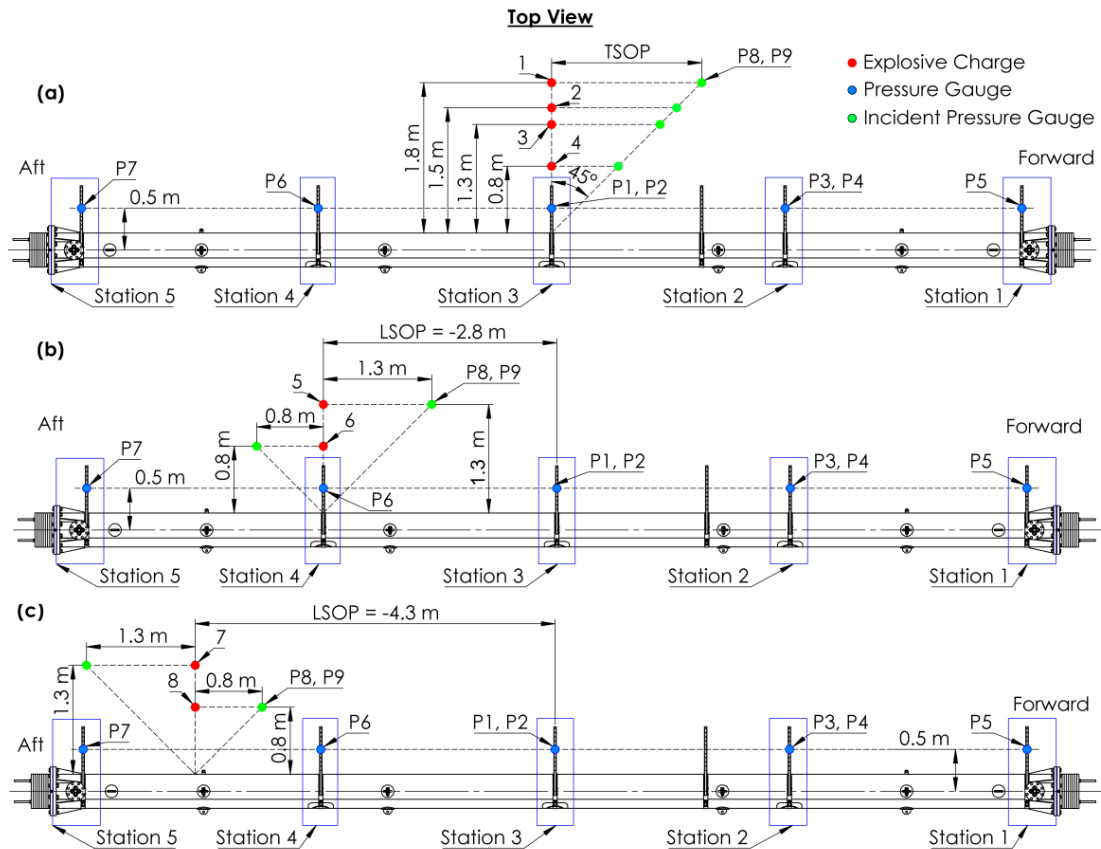


Figure 8: Topside view arrangement of charge location, external pressure gauges, and internal measurement locations for (a) Events 1 – 4, (b) Events 5 – 6, and (c) Events 7 – 8

Table 4: Details of event variables

Event	W (g)	TSOP (m)	LSOP (m)	Y
1	250	1.8	0.0	2.00
2	250	1.5	0.0	1.67
3	250	1.3	0.0	1.45
4	43	0.8	0.0	1.60
5	250	1.3	-2.8	1.45
6	43	0.8	-2.8	1.60
7	250	1.3	-4.3	1.45
8	43	0.8	-4.3	1.60

Events 1 – 3 used a 250 g charge at amidships (LSOP = 0), decreasing the TSOP distances for each successive event to establish the transition from borderline far-field to near-field UNDEX regimes. Event 4 used a smaller 43 g charge at amidships to investigate the effects of reduced explosive energy and bubble size on the platform’s response.

Events 5 and 6 repeated Events 3 and 4 at a LSOP of -2.8 m. These events were conducted to investigate BM2 of the platform. Events 7 and 8 also repeated Events 3 and 4, at a LSOP of -4.3 m. It was expected that these events would excite BM2 and BM3 of the platform and

reduce the contribution of BM1 due to the LSOP being aligned with the nodal location of BM1.

### 2.3. Measurement instrumentation

The full instrumentation outfit consisted of transducers for measuring the free-field water pressure, structural acceleration and velocity, and strain for each event. Measurements were taken at five measurement stations noted in Figure 8. This report only discusses the results of pressure and strain transducers to characterise the global whipping response from a structural perspective. Details of the additional data acquisition systems and transducers are discussed in Appendix A.

An Elsys TraNET data acquisition system [52] was used to sample pressure and strain transducers. The data acquisition system was located on shore and suspended transmission lines were run out to the platform over the water. All measurements were taken for a duration of four seconds post trigger time.

Outside the platform, nine free-field pressure gauges (P1 - P9) were suspended from the outriggers at locations noted in Figure 8. Two types of pressure gauges were used: Six PCB 138A05 [53] and three Neptune T11 [54] gauges. All Neptune T11 gauges were paired with a PCB 138A05 for comparison. The designations of each gauge type are listed in Table 5. All pressure gauges were suspended between the outriggers at fixed positions along the platform length to measure the spread of the incident pressure. Gauges P8 and P9 were moved in relation to the charge position for each event, as shown in Figure 8 and detailed in Tables 4 and 5, to measure the effective incident pressure at the stand-off point on the platform. All pressure gauges were sampled at 5 MHz to track the rise time of the shock wave as close as possible and calibrated to measure pressure relative to the ambient hydrostatic pressure of 0.05 MPa at the 5 m test depth ( $P_{\text{absolute}} = P_{\text{gauge}} + 0.05$ ).

Inside the platform, 24 weldable strain gauges (S1 - S24) were used to measure the hull structural response and monitor for any permanent deformation between events. Strain measurements were taken at four locations at approximately 90° increments around the hull circumference, at each of the five measurement stations shown in Figure 8. The exact locations of each strain gauge are described using a polar coordinate system shown in Figure 9, with the coordinates detailed in Table 5. Two strain gauge models were used: Six VPG CEA06-W250-350 [55] gauges were used in two 45° rosette arrangements at amidships on the portside (S1 - S3) and bottom (S4 - S6) as shown in Figure 9, and 18 TML AW-6-350-11-01LT [56] (S7 - S24) gauges were aligned in the axial direction. All strain gauges were sampled at 1 MHz with the Elsys TraNET data acquisition system. All internal gauge transmission lines exit the platform hull through topside cable glands, shown in Figure 5, where gauges at the forward end exit through the forward gland and gauges at the aft end exit through the aft gland. In most cases strain gauges that make up a planar response (athwartships of vertically opposite pairs) were not able to be positioned directly opposite one another. This means there will likely be some differences when the responses of these planar pairs are compared.

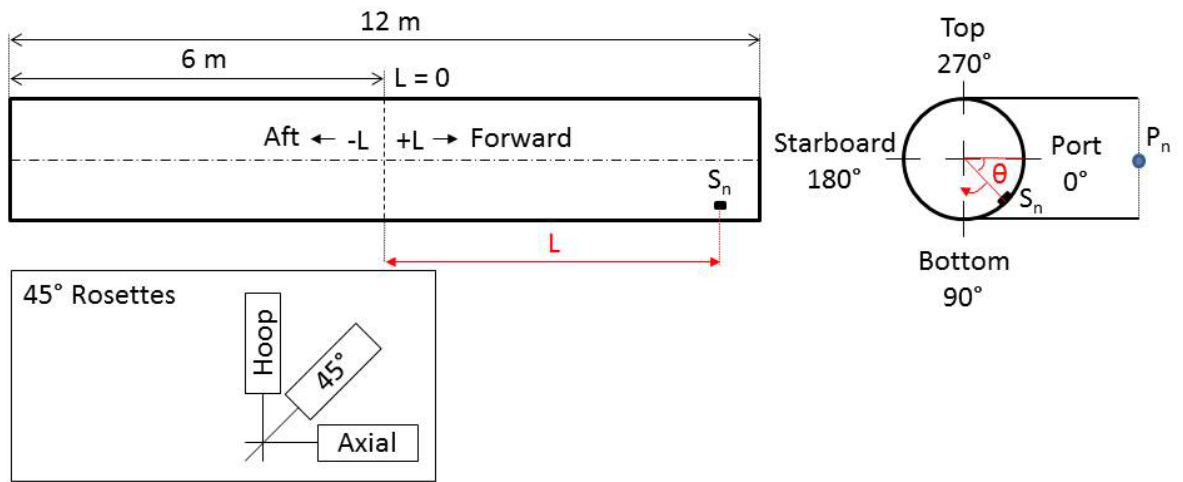


Figure 9: Internal arrangement of measurement transducers

Table 5: Strain and pressure gauge details and polar coordinates

Station	Gauge	L (mm)	$\theta$	Orientation	Model
1	S13	5825	353	Axial	TML
	S14	5735	90		
	S15	5890	187		
	S16	5890	270		
	P5	5640	0	-	PCB
2	S9	2750	0	Axial	TML
	S10	2850	90		
	S11	2500	180		
	S12	2800	270		
	P3	2800	0	-	PCB
	P4	2800	0	-	Neptune
3	S1	75	0	Hoop	VPG
	S2	75	0	Axial	
	S3	75	0	45°	
	S4	-50	90	Hoop	
	S5	-50	90	Axial	
	S6	-50	90	45°	
	S7	300	180	Axial	TML
	S8	0	270		
	P1	0	0	-	PCB
	P2	0	0	-	Neptune
4	S17	-2750	0	Axial	TML
	S18	-2850	90		
	S19	-2500	180		
	S20	-2800	270		
	P6	-2800	0	-	PCB
5	S21	-5825	353	Axial	TML
	S22	-5735	90		
	S23	-5890	187		
	S24	-5890	270		
	P7	-5640	0	-	PCB
-	P8	L = TSOP	0	-	PCB
-	P9	L = TSOP	0	-	Neptune

### 3 Results and discussion

The results obtained during the experimental investigation are presented and discussed under two general categories: incident pressure loading and structural response. The effects on the whipping response due to the TSOP, LSOP and charge mass are also discussed in further detail.

#### 3.1. Incident pressure

The incident pressures are representative of the pressure emitted by the explosive charge shock wave and bubble response at the measurement stand-off distance, where a positive pressure is defined as pushing away from the charge source and a negative pressure is pulling towards the charge source. These gauge pressure measurements are made relative to the ambient hydrostatic pressure of 0.05 MPa. Only one pressure gauge (P9) provided usable data from the experiments; all others suffered mechanical failure during the first few events. Gauge P9 ultimately failed in later events, which has been attributed to the repeated shock wave loading. Due to this, only measurements for Events 1 - 6 are presented and discussed in this section. No comparison of the different pressure gauge models is possible due to the gauge failures.

The characteristic incident pressure for all events consisted of the shock wave, followed by at least two significant bubble pulse cycles. Differences in the frequency of bubble pulsations were purely dependent on the charge size, as all events were conducted at the same depth of 5 m in this experiment. An example incident pressure record for the 250 g charge size from Event 1 is presented in Figure 10a. All 250 g events contained a minor third bubble response before the pressure record zeroes out, indicating the bubble has vented at the surface. The incident pressure for the smaller 43 g charge (example from Event 4 shown in Figure 10b) contained a third and fourth minor bubble pulse before the signal zeroed out. The additional minor pulse from the 43 g event is due to the smaller bubble produced, which builds up a lower buoyancy force and reduces the migration rate to the surface.

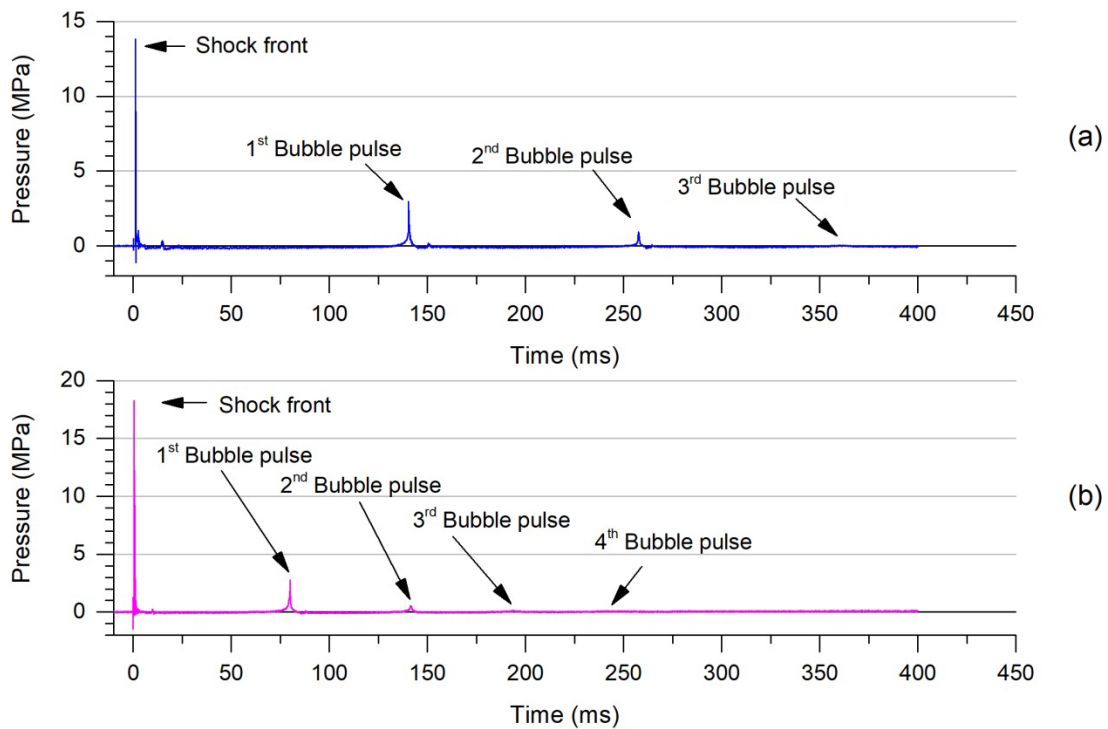


Figure 10: Characteristic incident pressures records for (a) 250 g charge from Event 1 (TSOP = 1.8 m) and (b) 43 g charge from Event 4 (TSOP = 0.8 m)

### 3.1.1 Shock wave

A detailed overview of the initial shock wave and reflection pressure loading is presented in Figure 11. The initial shock wave (Figure 11a) contained a small signal pulse almost immediately after the trigger time. This pulse was an artefact generated by the electric triggering mechanism and was present on all pressure and strain time histories and therefore, it was not considered to be representative of any mechanical loading from the UNDEX event itself. All pressure measurements of the initial shock wave contained large cavitation and collapse effects during the initial front decay. From the Time of Arrival (TOA) of the cavitation pulses, the source was determined to be from the outriggers that gauge P9 was suspended from. Because of this source, the measured cavitation loads are not representative of what was actually experienced on the platform. It is likely though that some cavitation would have occurred at the platform.

The later shock wave loads in Figure 11b were determined to be reflection sources from the platform (highlighted), free surface, and quarry floor and walls (highlighted), based on their TOA and relative distances from the gauge. The measured reflections from the platform are of course not representative of the direct loading experienced by the platform, but all other sources are considered to have contributed to the total shock loading of the UNDEX event.

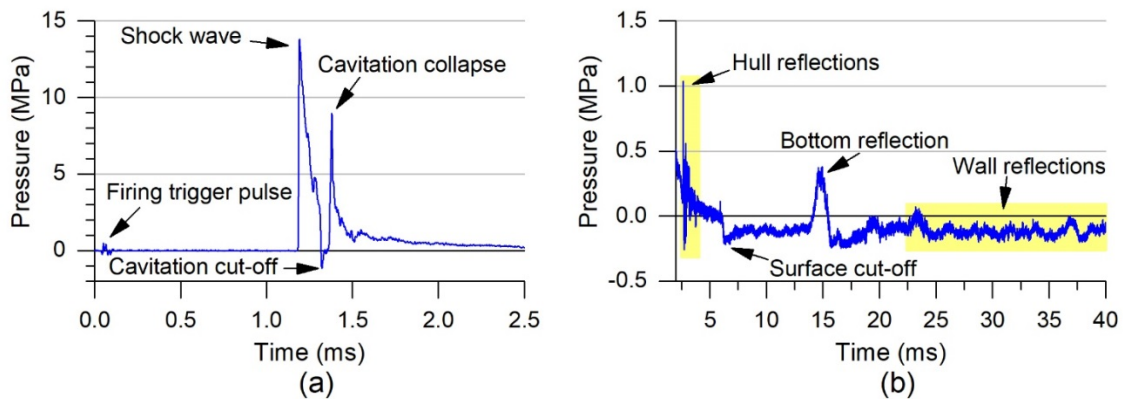


Figure 11: (a) Initial shock wave and (b) later shock reflection pressure measurements. Example from Event 1 (250 g, 1.8 m TSOP)

The initial shock wave incident pressure time histories from Events 1 – 6 are compared in Figure 12 for each charge size. The shock fronts from the 250 g charge events in Figure 12a show that the peak pressure increased when the TSOP distance was reduced, as expected. The measured cavitation loads from the outrigger in Event 1 were much larger than in other events. The variation in these loads can be attributed to variables in the outrigger design, such as bolt tension and fastening saddle position. Additionally, these outriggers did experience some plastic deformation from the first event which will have altered their response in subsequent events. Event 4 in Figure 12b also contained a more prominent cavitation loading from the outrigger than was seen in Event 6, which may be due to further plastic damage occurring from this closer event.

There was a slight difference in TOA between Events 3 and 5 which have the same TSOP distance. There was a standard error of 3.4% between their arrivals which can be accounted for within the charge placement tolerance. The similar 43 g charge Events 4 and 6 also had a difference in TOA with a larger standard error of 8.8%, which can also be accounted for in the charge placement tolerance.

There was excellent comparability of the peak pressure between the similar events with an average peak pressure of 21.8 MPa and standard error of 0.1% for 250 g Events 3 and 5, and average peak pressure of 18.1 MPa with a standard error of 0.8% for the 43 g Events 4 and 6. The close similarity of the peak shock wave pressure shows that the noticeable difference in TOA did not have a significant impact on the shock loading. The close similarity of these events also suggests that the shock loads of Events 7 and 8, which did not produce reliable measurements, can be assumed to be similar to Events 3 and 5, and Events 4 and 6 respectively.

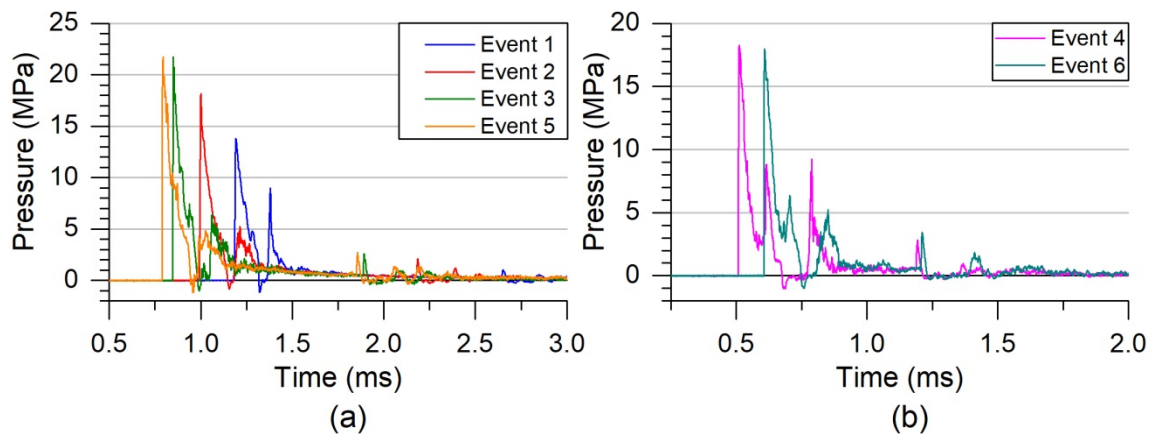


Figure 12: Comparisons of the initial shock wave for Events 1 – 6 for (a) 250 g and (b) 43 g charge sizes

### 3.1.2 Bubble response

The characteristic response of one bubble cycle (example from Event 1) is presented in Figure 13. Here it is shown that the gauge pressure was mostly negative during the quarry wall and floor reflections from the shock wave. The pressure record steadied and further reduced after these reflection sources, which is the characteristic response of the bubble under-pressure phase from its expansion. The lowest pressure followed by a steady increase indicated when the bubble had reached its maximum radius, noted in Figure 13a by the dashed line. The pressure steadily increased until it reached the hydrostatic pressure, and then it increased rapidly into the bubble pulse, highlighted in yellow. A close-up of the bubble pulse incident pressure in Figure 13b shows that the regular pulse shape had a sharp peak. The near instantaneous rise time of this peak indicates that a shock wave was emitted during the collapse phase of the bubble cycle and therefore this collapse partially occurred at supersonic velocity in the water. The highlighted bubble pulse rapidly decays and was followed by the arrival of its own surface cut-off reflection wave, and then the reflection from the quarry floor. The pressure then stabilised at the hydrostatic pressure until the bubble began to expand again, and the cycle was repeated.

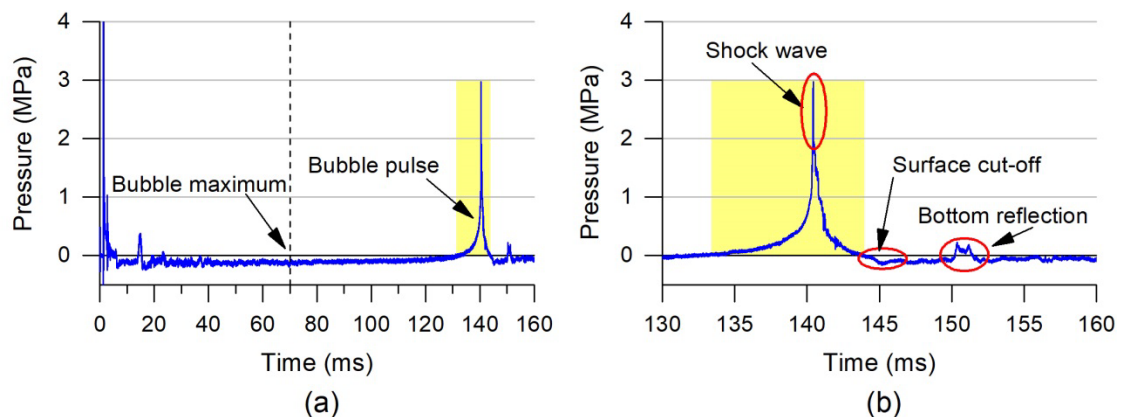


Figure 13: Incident pressure due to the pulsating bubble noting (a) the bubble maximum and pulse, and (b) the loading from the bubble pulse. Example from Event 1.

A comparison of the significant first and second bubble pulses from Events 1 – 6 is presented in Figure 14 for each charge size. The periods and frequencies of each bubble cycle are listed in Table 6. The period of each cycle is taken as the time between the peak of the shock wave to the peak of the first bubble pulse for  $T_1$ , and from the peak of the first bubble pulse to the second bubble pulse for  $T_2$ . The plots in Figure 14 contain offsets for their transmission time from the charge to the platform and so the time values in Figure 14 are not a direct measurement of the period.

The first bubble pulse of the 250 g charge Events 1 – 3 and 5 are presented in Figure 14a, and show that the pulse shape of all these events was very similar and all emitted a shock wave at the peak of the bubble pulse. The average period of these events was calculated as 138.5 ms with a standard error of 0.2%, which compares very well with the predicted value from Equation 1.1 of 140 ms. Generally the peak pulse pressure increased between events as the TSOP distance was reduced, but unexpectedly Event 2 had the highest peak pressure due to its shock wave. This may be due to some variation in the expansion rate of the recompressed explosive gas. However, if the shock wave component of the bubble collapse is ignored, the overall pressure pulse from Events 3 and 5 was larger. Events 3 and 5, which had the same stand-off distance of 1.3 m, had good correlation with their TOA and pulse magnitudes, where the average peak of these similar events was 3.9 MPa with a standard error of 5.6%.

The first bubble pulse of the 43 g charge Events 4 and 6 presented in Figure 14b, also had very good similarity in their pulse shape and magnitude. The period of both events was 79 ms, and corresponds to a pulsation frequency of 12.7 Hz, which compares well to the predicted 12.8 Hz from Equation 1.1. The average pulse peak pressure was 2.9 MPa with a standard error of 4.5%. Unlike the 250 g events, these bubble pulses did not contain a shock wave component, which indicates the bubble collapse was entirely subsonic. The different response seen between charge sizes is likely due to the greater amount of energy that is contained in the 250 g charge compared to the much smaller 43 g charge.

The second bubble pulses are presented in Figure 14c for 250 g and Figure 14d for 43 g events. Events 3 and 4 were found to have much smaller and flatter pulse shapes than their respective similar Events 5 and 6. However, Event 3 did contain a short spike right before the pulse begins to decay. While the pulse shapes varied, the spike in Event 3 meant that the peak pulse pressures of Events 3 and 5 compared well, with an average of peak pressure of 1.1 MPa and standard error of 3.1%. The similar 43 g Events 4 and 6 at the same stand-off distance of 0.8 m did not compare well, with a large standard error of 24.9% between the two results. The flattened pulse shape of Event 4 was unusual and the experimental setup did not provide a sufficient way to track the shape and motion of the bubble. Based on other experimental work, as discussed in section 1.1, a combination of interaction with the platform and migration of the bubble could be responsible for the distorted pulse profiles seen in both Events 3 and 4.

The average second bubble cycle period for the 250 g events was 116 ms with a standard error of 0.4%, corresponding to a pulsation frequency of 8.6 Hz. For both 43 g events, the period was 61 ms, corresponding to a frequency of 16.4 Hz. A reduction in period between each pulsation cycle was expected due to the loss of energy that is emitted at the bubble pulse, which reduces the maximum size the bubble can reach. However, it was found that

the periods did not reduce as much as predicted from Equation 1.1 in Table 3, where the 250 g and 43 g second bubble cycle periods were predicted at 106 ms and 59 ms respectively. The error is consistent between events of similar charge size, with the second cycle period being approximately 9% and 4% longer than predicted for the 250 g and 43 g charges respectively. Two possible causes for this deviation have been identified: Firstly, the sample size for Pentolite UNDEX bubble data beyond the first bubble cycle from Swift and Decius [5] is limited to only two results, and the depth and charge sizes of the present investigation are outside of the ranges of the dataset. Secondly, if the predictions are accurate for free-field UNDEX, the apparent increase of the second bubble period may be taken as evidence of Bjerknæs repulsion forces, which would indicate the bubble “sees” the whipping hull as a flexible boundary during the second cycle. Under the circumstances of this second possibility, the closer relative size of the bubble radius to the platform radius during the second cycle may have also increased the coupling strength of this bubble-structure interaction. However, the sample size of these results is insufficient to draw a conclusion to the exact cause.

The bubble period coefficients for the first  $K_1$  and second  $K_2$  bubble cycles have been calculated for all measured events in Table 6. An overall average of the first bubble period coefficient  $K_1 = 2.12$  from these experiments compares well to the  $K_1 = 2.11$  value from Swisdak [4]. Closer examination of individual events shows that the two furthest events 1 and 2 from the platform (250 g at 1.8 m, and 1.5 m) matched Swisdak’s value, while the two 250 g Events 3 and 5 at 1.3 m stand-off had a lower value of  $K_1 = 2.09$ . The smaller 43 g charge Events 4 and 6 at the closer stand-off distance of 0.8 m had a larger value of  $K_1 = 2.15$ . These different values result from events outside of the general far-field assumption of  $\gamma > 2$  which is considered as a limitation of the similitude equations. The results of the present experiment indicate that similitude predictions from Equation 1.1 were valid when  $\gamma > 1.67$ . Beyond this limit the predictions were unreliable and given the counteracting variation between the smaller and larger charge size scenarios, further work is required to understand the influence of charge size and stand-off distance variables on the fluid-structure interaction. Underwater imaging may greatly assist in future investigations of the bubble-structure interaction.

As previously discussed there was a large deviation of the expected second bubble period predictions and the present experimental results. Therefore, the overall average measured second bubble period coefficient of  $K_2 = 1.73$  also varied significantly from the average Swift and Decius [5] value of  $K_2 = 1.59$ . For the second bubble period, only the charge size seems to have influenced the bubble period where for the 250 g charge an average  $K_2 = 1.76$  was measured, while for the smaller 43 g charge an average  $K_2 = 1.66$  was measured. This suggests that during the second bubble period the stand-off distance and therefore the relative proximity  $\gamma$  did not have a significant effect on the pulsation period. The same issue of different coefficients between the charge sizes is still present, and further work would be required to establish the effects of charge size on the bubble-structure interaction where  $\gamma < 1.67$ . Migration of the bubble between pulses may also account for differences in the period and  $K$  factors. Without observation of the bubble response there was no way to determine the contribution of migration to this effect. Given the data from this experiment is of a larger sample size of pentolite explosives than what is present in Swift and Decius [5], the presented second bubble period coefficients from this

investigation may be more suitable for use in similitude equations on similar scenarios. For future exploration, free-field UNDEX measurements as a baseline may provide insight on the bubble-structure interaction effects.

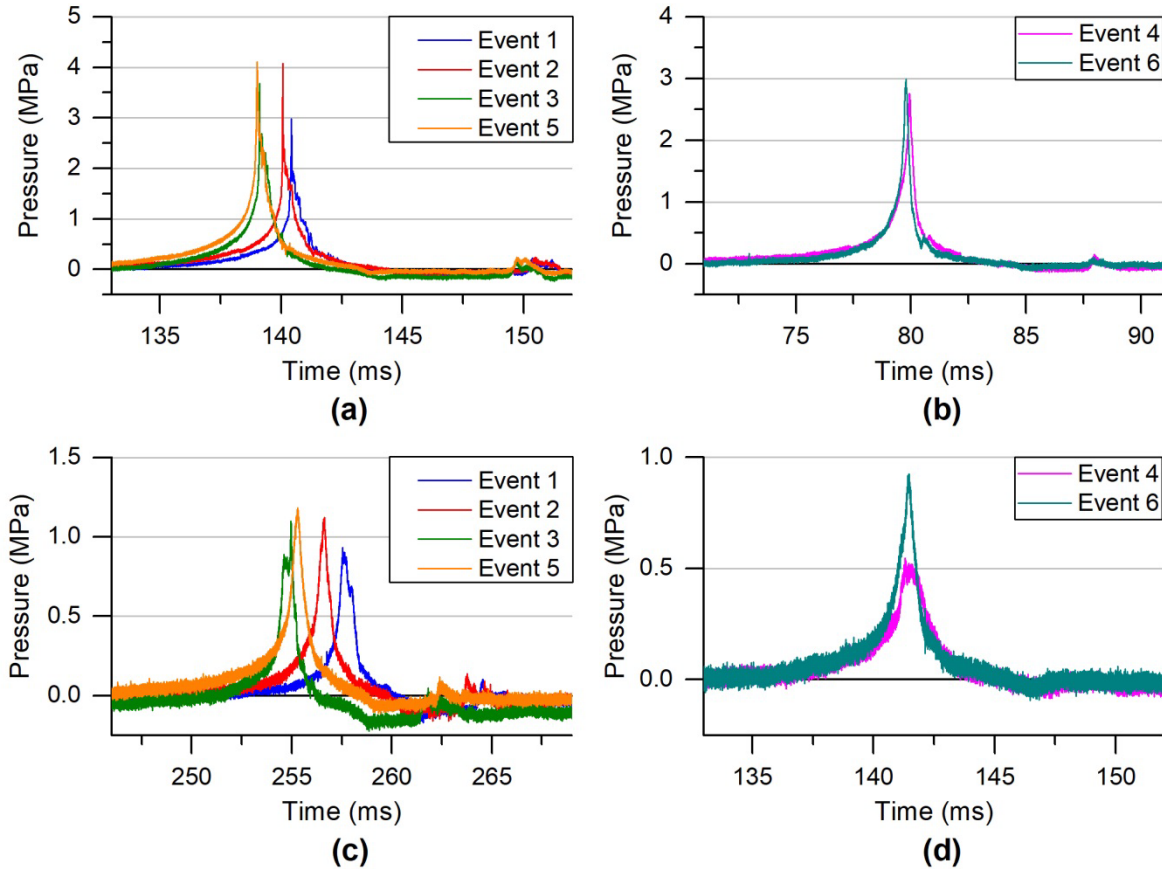


Figure 14: Comparison of (a) the first bubble pulse for 250 g, (b) 43 g, and (c) the second bubble pulse for 250 g and (d) 43 g charge sizes from Events 1 – 6

Table 6: Bubble periods pulsation periods for the first and second cycles for Events 1 – 6

Event	$T_1$ (ms)	$T_2$ (ms)	$f_1$ (Hz)	$f_2$ (Hz)	$K_1$	$K_2$
1	139	117	7.2	8.5	2.11	1.77
2	139	116	7.2	8.6	2.11	1.76
3	138	115	7.2	8.7	2.09	1.74
4	79	61	12.7	16.4	2.15	1.66
5	138	116	7.2	8.6	2.09	1.76
6	79	61	12.7	16.4	2.15	1.66

### 3.1.3 Pressure impulse

To assess the contribution of the shock wave and bubble components, the pressure impulse of each event was calculated from the pressure-time histories using Equation 1.2. An example of the first bubble cycle impulse from Event 1 is presented in Figure 15. The total pressure impulse of the event  $I_T$  (highlighted in yellow) is the absolute sum of the

maximum shock impulse  $I_S$  and the positive  $+I_B$  and negative  $-I_B$  portions of the bubble under-pressure impulse  $I_B$ . The start of the bubble pressure impulse is determined by a significant change in gradient after the shock wave reflection arrivals, denoted by the first dashed line in Figure 15. This point is noted for the 250 g and 43 g charges presented in Figure 16. It is shown that there is a notable delay between the initial shock wave loading and the onset of the bubble under-pressure loading due to the comparatively slower response of the explosive gas expansion rate for the bubble.

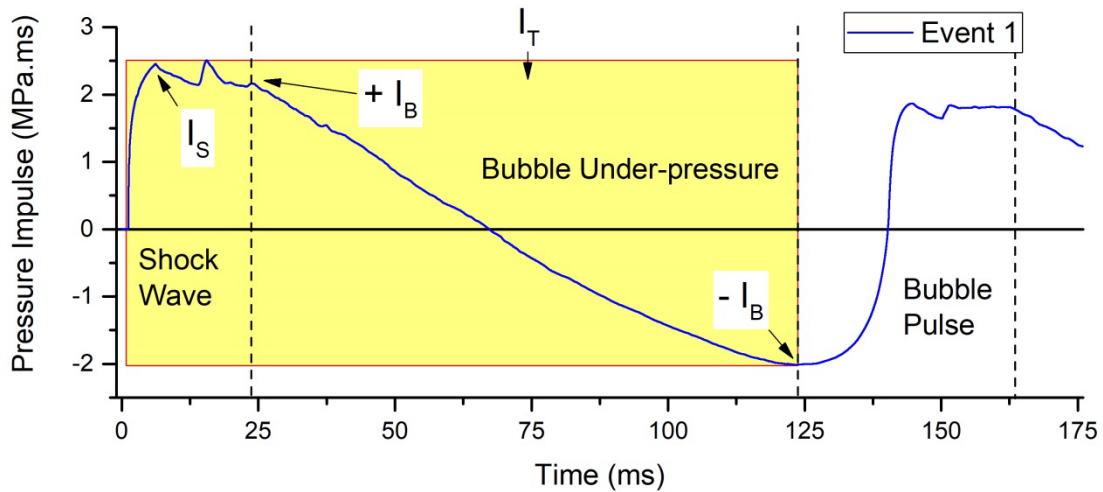


Figure 15: Example of pressure impulse produced by Equation 1.2 from Event 1 incident pressure

From the identified delay between the shock front and first bubble expansion, a cut-off point between shock loading and bubble loading components was defined. For all 250 g charges, bubble impulse was insignificant on the structure for the first 24 ms, while for 43 g charges there was insignificant bubble impulse for the first 12 ms. Based on these observations, these times were taken as the points at which initial shock loading had ceased and the bubble loading became dominant. This point is noted for each charge size in Figure 16 by the dashed line.

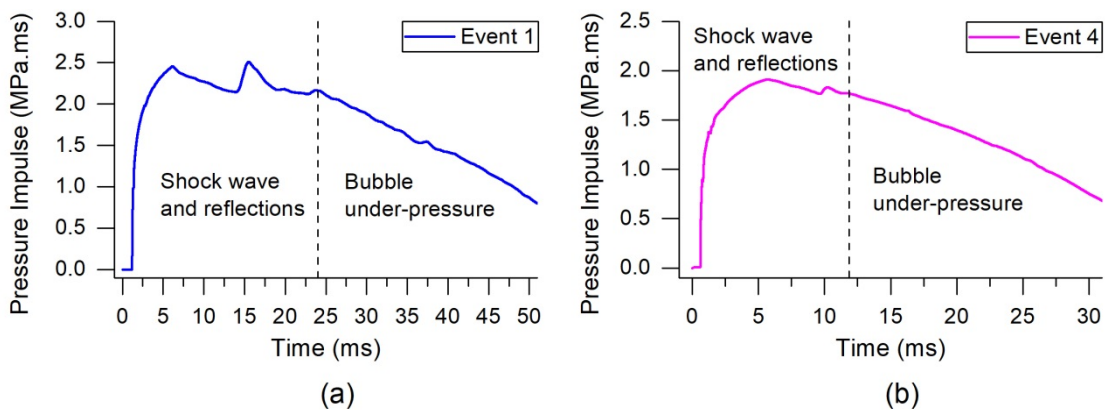


Figure 16: Pressure impulse near the end of the shock front and beginning of bubble loading for the (a) 250 g and (b) 43 g charge sizes.

The pressure impulse magnitudes for the  $I_S$  and  $I_B$  of each event are listed in Table 7. Assessing the relative contribution of  $I_S$  and  $I_B$  on the  $I_T$  it is shown that the average percentage of  $I_S$  and  $I_B$  is respectively 35.1% and 64.9% of  $I_T$  across all measured events, with a standard error of 0.6%. Given the different variables in charge mass and stand-off distance of each event, such consistency in these pressure impulse contributions between events indicates that this is likely a property of the explosive material.

For similar events with the same charge sizes and stand-off distances, the standard error of the total impulse was 3% for 250 g at 1.3 m stand-off and 1% for 43 g at 0.8 m stand-off. Based on the similarity of these pressure impulses and the previously noted similarity of the distribution of the shock and bubble pressure impulses, it was assumed that Events 7 and 8 would have likely had similar incident pressure time histories for their respectively similar charge sizes and stand-offs. Calculated results of  $I_T$  for Events 7 and 8 have been produced by the average values of similar events. The breakdown of  $I_S$  and  $I_B$  has been calculated assuming the previously noted average percentage contributions of  $I_T$  and these results are listed in Table 7.

Table 7: Pressure impulse magnitudes for shock and bubble components

Event	$I_S$	$I_B$	$I_T$	$I_S/I_T$	$I_B/I_T$
1	2.45	4.19	6.64	36.9%	63.1%
2	2.88	5.23	8.11	35.5%	64.5%
3	3.32	5.96	9.28	35.8%	64.2%
4	1.74	3.64	5.38	32.3%	67.7%
5	3.44	6.43	9.87	34.9%	65.1%
6	1.91	3.55	5.46	35.0%	65.0%
Average				35.1%	64.9%
7	3.36	6.21	9.57	-	-
8	1.90	3.52	5.42	-	-

### 3.2. Structural response

The results and discussion of the structural response are categorised by whether the shock or bubble loading initiated the response. From the previous discussion of the pressure impulse loading, the cut-off point between shock and bubble loading was defined as 24 ms and 12 ms from detonation for the 250 g and 43 g charges respectively. Therefore, any structural response between detonation time and the defined cut-off time for each charge size is assumed to be due to the shock loading, while any response after this cut-off time is assumed to be due to the bubble loading.

For the presented strain records, positive strain is defined as a tensile response and negative strain is a compressive response. All presented transient strain records were decimated by a factor of six with a moving-average filter to reduce the signal noise. Strain records presented for bubble loading responses were further filtered by the application of a low pass 10 kHz Fast Fourier Transform (FFT) filter to further reduce noise. Shock responses are presented unfiltered due to their large frequency content and short duration. As with the pressure measurements, all strain records contain a trigger signal pulse

artefact shortly after the trigger time due to the electric trigger mechanism, which is not a mechanical response.

The first strain responses arise from the shock wave impact at the gauges closest to the stand-off point on the platform. An example of this from the amidships rosette arrangement on the portside for Event 1 is presented in Figure 17. The first measurement is a small and short duration compressive response from all gauges, indicating this is a local “dishing” reaction of the platform hull. This is followed by a rapid series of high magnitude tensile and compressive response cycles (highlighted in yellow), for an overall duration of approximately 0.25 ms. The early TOA and duration of this loading is likely due to cavitation formation and collapse around the stand-off point (SOP) from the shock wave induced motion and elastic deformation of the platform hull, as well as the interaction of incident and reflection pressure waves in the surrounding fluid. In all events, this cavitation response cycle was the most severe response from the shock loading. After the cavitation loading, the platform begins to undergo a global structural response, with the first minor bending response occurring around 0.25 ms after the cavitation response, noted in Figure 17.

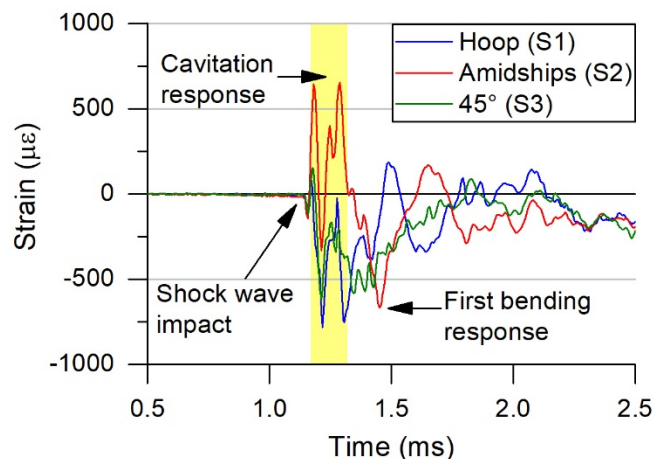


Figure 17: Strain measurements of the initial shock response from gauges S1 – S3 in a rosette arrangement at amidships. Example from Event 1 (250 g, 1.3 m TSOP).

At measurement locations away from the SOP, the initial strain response was different. It was observed from strain measurements taken around the -2.8 m aft station (strain gauges S17 – S20) in Figure 18a, that all four gauges contained a similar compressive pulse response at the same time. Based on this behaviour and the TOA, this first response was determined to be caused by the stress wave propagating down the cylinder from the initial SOP. This wave arrives before the water-borne shock wave because it is travelling at a higher acoustic velocity of 5000 m/s through steel. This signal is followed a short time later by the arrival of the water-borne shock wave, noted in Figure 18a. Comparing the response as the shock wave moves down the hull length from gauges at amidships (S2), -2.8 m aft (S17), and -6 m aft (S21) in Figure 18b, it is shown that the water-borne wave response amplitude reduces at gauges further from the initial SOP. This is due to the greater distance the wave must travel, and therefore disperse, as well as the increased perpendicular angle of incidence of the shock wave interacting with the hull. In contrast,

the steel-borne stress wave maintains a similar amplitude between strain gauges S17 and S21 as it moves along the hull length from the initial SOP, due to the absence of the larger dispersion area and angle of incidence that are present in the water environment.

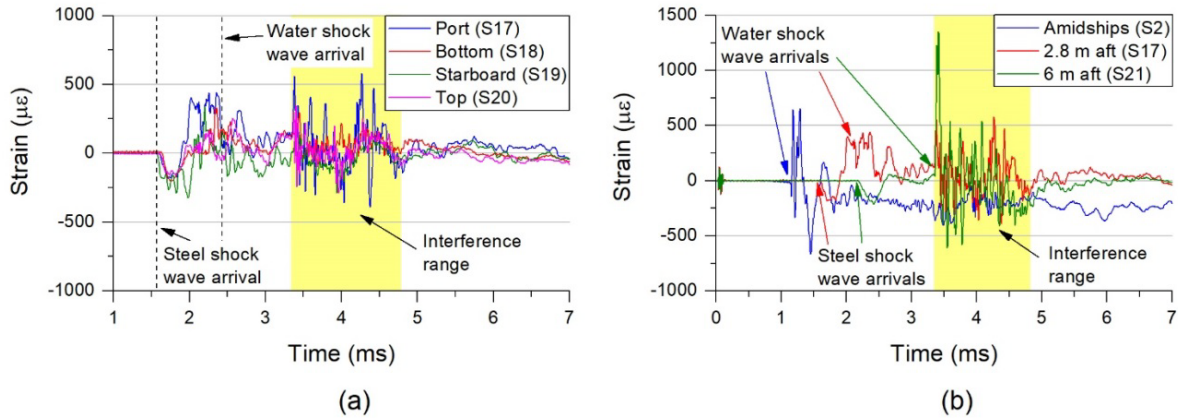


Figure 18: (a) Strain measurements for the shock response at -2.8 m aft (S17 – S20), showing the TOA for the steel and water acoustic waves, and interference range. (b) Strain measurements for the portside shock response at amidships (S2), -2.8 m aft (S17) and -6 m aft (S21), showing the different TOA for the steel and water shock waves, and the simultaneous arrival of interference. Example taken from Event 1 (250 g, 1.3 m TSOP)

The arrival of the water-borne wave at bow and stern locations, noted when the water shock wave arrived at strain gauge S21 in Figure 18b, coincided with a significant high frequency anomaly (highlighted in yellow) that was found to be present in many of the strain records. This interference level greatly exceeds the initial shock wave response strain levels at the SOP on most gauges. In some cases the increase in strain is greater than twice the yield strain limit of the material. Notably in Figure 18b, this interference has the same TOA on all affected strain gauges, regardless of their location from the initial SOP. Therefore, this interference cannot be due to a localised event around any one gauge, but must be due to a disturbance in the transducer and data acquisition arrangement used by these gauges. Based on the TOA of the interference signal, it was determined that this interference is likely due to the shock wave impacting and reflecting amongst the measurement cables that protrude from the cable glands on the top side of the platform, shown in Figure 5. The rapid squeezing and release of the cable may have caused an unwanted change in the cable electrical resistance, acting in series with the desired signals from the strain gauges. The phenomenon has been observed and discussed by Walter [57] as a known problem in shock test measurements. This interference was greater at the aft cable protrusion, which may be attributed to a variation in the cable sealing process. On post-experimental examination, it was found the cables protruding closest to portside (the same side as charge detonation) were affected more than those closest to the starboard side, with the portside cables likely “shielding” those on the starboard side to some degree. For most strain measurements, the TOA of the interference was outside of any significant loading or structural response time ranges of interest and therefore, the interference response could be neglected. For measurements taken at the bow and stern of the cylinder (strain gauges S13 – S16 and S21 – S24) this was not the case, as these gauges were located near the cable gland protrusion and the shock wave reached these areas in

the same time frame. To report the true maximum strain of the affected locations, it was assumed that due to the spherical spreading from the near-field UNDEX source, the angle of incidence of the shock wave perpendicular to the hull at bow and stern locations was very large, and the bending strain in these areas was minimal due to the free-free beam structure. Therefore, it was assumed that the greatest strain response due to shock loading at these locations would be due to the strain wave travelling through the platform, and not the apparent maximum within the interference range.

For the strain response due to bubble loading and damped free-vibration of the platform, the principal plane (vertical or athwartships) of the response was determined by comparing the axial strain gauge measurements about a single measurement location. An example from Event 1 taken at the amidships axial strain gauges (S2, S5, S7, and S8) and presented in Figure 19 demonstrates that the primary response was bending in the athwartships plane (strain gauges S2 and S7). This was also the primary response plane for all events in this experiment. It was found that all portside gauges measured larger peak strain levels than their starboard counterparts, by an average of  $91 \mu\epsilon$  in all events. There are three main reasons why this was the case. First, the mass distribution between the port and starboard sides of the platform was not equivalent. The starboard side access porthole reinforced cut-outs were heavier than the portside mounted outriggers which resulted in a noticeable angle of list of  $7^\circ$  to starboard. The heavier starboard side will have naturally been more resistant to any induced motion of the platform and the port side is also closer to the loading source. Second, the strain gauges on opposite sides (port – starboard, top – bottom) were not always directly opposite one another. For low frequency bending responses this was not as significant an issue due to the proportionally larger wavelength. However when higher frequency bending responses were present, the strain gauge pair misalignments were more noticeable due to the shorter wavelengths. Larger differences were observed in these scenarios, but these were due to phase misalignment from the gauge measurements as opposed to different amplitudes. Finally, the presence of a bending response in the vertical plane, as seen in Figure 19 indicates that the platform response was three dimensional and therefore the measurements at each gauge will not be purely from axial strain due to in-plane bending. The vertical bending responses were found to be of a similar order of magnitude as the differences seen in the port and starboard measurements.

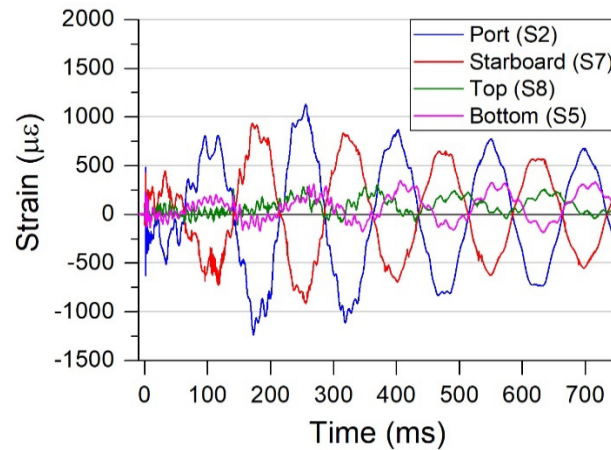


Figure 19: Strain measurements of the response from bubble loading at amidships (gauges S2, S5, S7 and S8) demonstrating the primary bending response in the athwartships direction. Example from Event 1 (250 g, 1.3 m TSOP).

### 3.2.1 The effect of transverse stand-off distance

To determine the effect that the TSOP has on the structural response, the amidships stand-off (LSOP = 0) Events 1 - 4 are considered. A summary of the largest strain response magnitudes at each section of the platform for these events, due to shock and bubble loading, is presented in Figure 20.

The shock response was largest at amidships for all these events, and was lower at measurement points further along the hull in both forward and aft directions, with the bow and stern locations exhibiting the lowest responses. This was expected due to the spherical spreading and increasing perpendicular angle of incidence to the hull of the shock wave.

For both shock and bubble loading, only minor strain responses were measured at the bow and stern locations, where the greatest strain of the four events was 232  $\mu\epsilon$  measured during the shock response at the stern during Event 3. Given the free-free ended boundary condition of the platform, it was expected that these locations would be more susceptible to direct shock loading than from any global bending response initiated by the bubble loading. All events demonstrated this to be the case, though the response from shock loading was only marginally higher than that from bubble loading. It should be reiterated here that the mass distribution at the bow and stern is much higher than along the cylindrical hull, due to the flanges and end mass plates which account for approximately 22% of the overall platform mass at each end. Due to this design, the platform was inherently more resistant to dynamic effects at these locations.

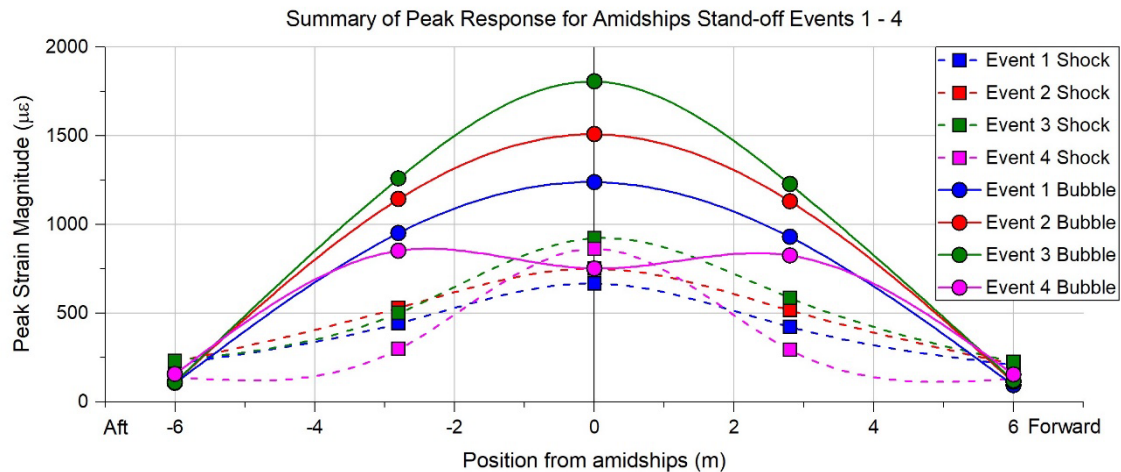


Figure 20: Largest strain response magnitudes due to shock and bubble loading at each measurement point for amidships SOP Events 1 – 4.

For 250 g Events 1 – 3, the largest strain response from bubble loading occurred at amidships on portside, and like the shock wave response the strain levels were lower at measurement points further along the hull in the forward and aft directions, with the lowest response seen at the bow and stern locations. The distribution of the response due to bubble loading indicated global bending of the platform as the dominant response. The most severe event of these three events, as well as overall of events conducted, was Event 3, at the closest TSOP of 1.3 m. In the event, the peak strain response at amidships was measured as 1806  $\mu\epsilon$ , which slightly exceeds the theoretical static yield limit of 1750  $\mu\epsilon$ . However, all strain gauges at the amidships location had no indication of physical yielding occurring. For all amidships 250 g events, the peak response from bubble loading was an average of 94% larger than the peak response from shock loading, therefore the bending response from the bubble loading is the dominant response of these three UNDEX events.

Comparing the bubble response of these three events at amidships from the strain gauge closest to the SOP (S2) in Figure 21a, it is shown that the bending response in the platform was amplified and the peak strain response occurred just after the first bubble pulse. This amplification of bending is a clear indication that a whipping response was induced by the UNDEX events. The bending strains are generally maintained up to the second bubble pulse, with an average reduction in strain levels of 11 %. Notably the closest Event 3 had a significantly larger reduction of 308  $\mu\epsilon$ , compared to 105  $\mu\epsilon$  for Event 1 and 109  $\mu\epsilon$  for Event 2. This larger reduction in Event 3 did not continue in successive bending responses but was sufficient enough to make the bending responses after the second bubble pulse for Events 2 and 3 almost equivalent. This unique behaviour in Event 3 suggests that the closer proximity of the bubble to the structure had a significant effect on the severity of the whipping response, and this severity was increased only when the bubble was forcing the bending response in the platform over the first bubble cycle.

After the second bubble pulse, the platform demonstrated a damped vibration response that follows an exponential decay, which suggests the bubble loading was no longer strong enough to have any significant effect on the platform's response. High frequency

components from the shock wave loading were almost completely damped out by this time and the response is dominated by only a single modal frequency.

The frequency of the whipping response observed in these three events was determined by performing a FFT on the transient signals in Figure 21a to produce a frequency response plot, presented in Figure 21b. All frequency response plots presented in this paper were produced from an FFT performed on the full length and raw strain record, with a duration of 4 seconds at a sampling rate of 1 MHz. From this plot it was found that the whipping response was dominated by a single frequency of 6.7 Hz. Comparing this to the initial modal analysis from Table 1, the response was identified as the first bending mode (BM1) of the platform.

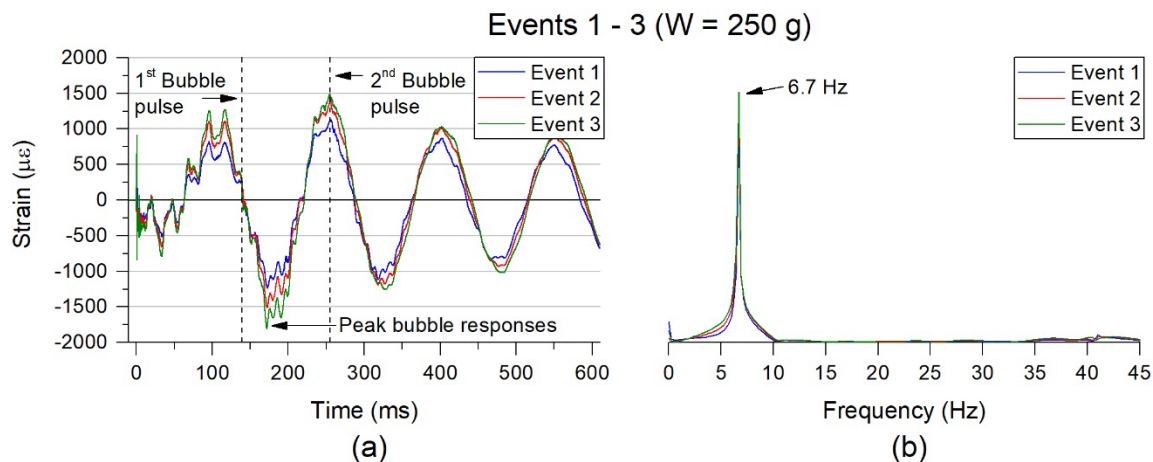


Figure 21: (a) Comparison of the strain response from bubble loading at amidships (S2) for Events 1 - 3. (b) Frequency response FFT plot of these records.

The 43 g Event 4 at 0.8 m TSOP differed in its bubble loading response from the other amidships events, where the greatest bubble response was measured at the portside locations 2.8 m forward and aft of amidships. The largest bubble response was also slightly lower than the shock response for this event. From the transient strain records on portside at the amidships (S2), 2.8 m forward (S9) and aft (S17) measurement locations, shown in Figure 22a, it was found that there was a higher frequency component in the whipping response. The frequency response of these signals, shown in Figure 22b, revealed that all these locations contained two significant frequency responses: a dominant response at 6.7 Hz, which was previously identified as the BM1 response of the platform, and another response at 41 Hz. From the modal analysis in Table 1, the 41 Hz response was identified as the third bending mode (BM3) of the platform. BM1 and BM3 share a peak response at amidships and the altering phase of these responses resulted in alternating constructive and destructive interference between amidships and the 2.8 m forward and aft measurement locations. The arrival of the first bubble pulse coincided with the first peak of the BM1 response, as noted in Figure 22a, and the UNDEX induced whipping response amplified the interaction between BM1 and BM3. The timing of this bending mode interaction resulted in a constructive response occurring at the 2.8 m forward and aft locations for the maximum measured response due to the bubble loading, and a destructive response at amidships. Notably, this response only occurred under the driving force of the first bubble cycle, and after the first bubble pulse the largest bending

response consistently occurred at amidships. The amplified response during the bubble loading is again indicative of UNDEX induced whipping. It is also worth noting the bending responses at the 2.8 m forward and aft locations are in phase and have almost exactly the same amplitude over the entire response duration which indicates the platform's response was symmetrical about amidships. Therefore under this scenario the platform exhibited two independent zones of high severity while its response was driven by the first bubble cycle.

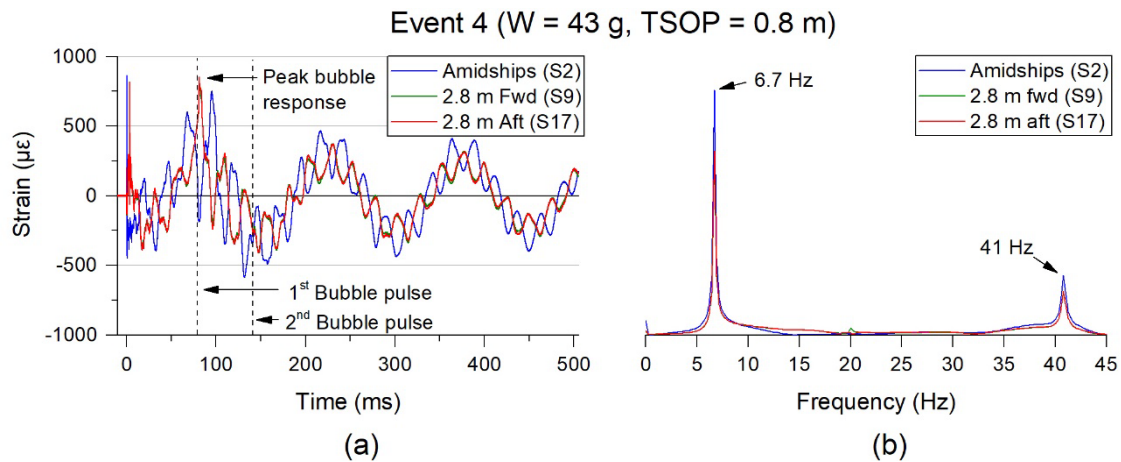


Figure 22: (a) Strain response from bubble loading at portside amidships (S2) and 2.8 m forward (S9) and aft (S17) from Event 4. (b) Frequency response plot of these records.

### 3.2.2 The effect of longitudinal stand-off position

To examine the effect that different charge LSOPs had on the platform's response, Events 3 – 8 are considered. These events are discussed according to their similar charge size and TSOPs. Initially the results of events with a 250 g charge size at a 1.3 m TSOP (Events 3, 5, and 7) are considered. A summary of the largest peak strain response magnitudes along the platform length from shock and bubble loads in these events is presented in Figure 23.

The peak strain measured for the initial shock response of the platform was found to have a similar severity at the station closest to the SOP for each event, with a maximum shock response of 923  $\mu\epsilon$  in Event 3 and 816  $\mu\epsilon$  in Event 5. For Event 7, there was no strain gauge at the direct SOP. At 2.8 m aft a peak strain of 871  $\mu\epsilon$  was measured, while the closer proximity of the charge to the cable protrusion produced substantial interference on the signals of all strain gauges near the stern (S21 – S24) and no reliable measurement of the shock response could be obtained. The trend of the maximum shock response along the hull length for Event 7 indicates the peak response may have been higher than what was measured at 2.8 m aft, and would have occurred between the 2.8 m aft and stern measurement locations. However, the similarity of the peak strain level at 2.8 m aft compared to other events suggests that it would not have been significantly higher at other locations. The measured results have good correlation despite the issues with Event 7, with an average peak strain of 870  $\mu\epsilon$  and standard error of 3.5% over the three events. Therefore for these events, the shock response was not affected by the LSOP. The distribution of the shock response along the platform length for Events 5 and 7 was similar

to what was observed in Event 3, with the peak of the distribution only being offset along the platform length by the change in LSOP in each of these events.

Similar to what was observed in Events 1 - 4 in Figure 20, only minor strain responses were measured at the bow and stern locations for Events 3, 5, and 7 in Figure 23, where the greatest strain measured was  $467 \mu\epsilon$  at the stern during the shock response of Event 5. It is worth reiterating that it is likely the shock response at the stern would have been larger during Event 7 given its LSOP distance was the closest to this location, but reliable measurements could not be obtained at this location due to signal interference. As previously discussed this general distribution was expected due to the charge proximity, mass distribution and free-free ended boundary condition of the submerged platform. Unlike the amidships events, the peak responses of Events 5 and 7 were larger at the stern than the bow for both the shock and bubble responses. This can be attributed to the closer proximity of the charge, and smaller perpendicular angles of incidence from the spherically spreading shock and bubble pulse waves for these events.

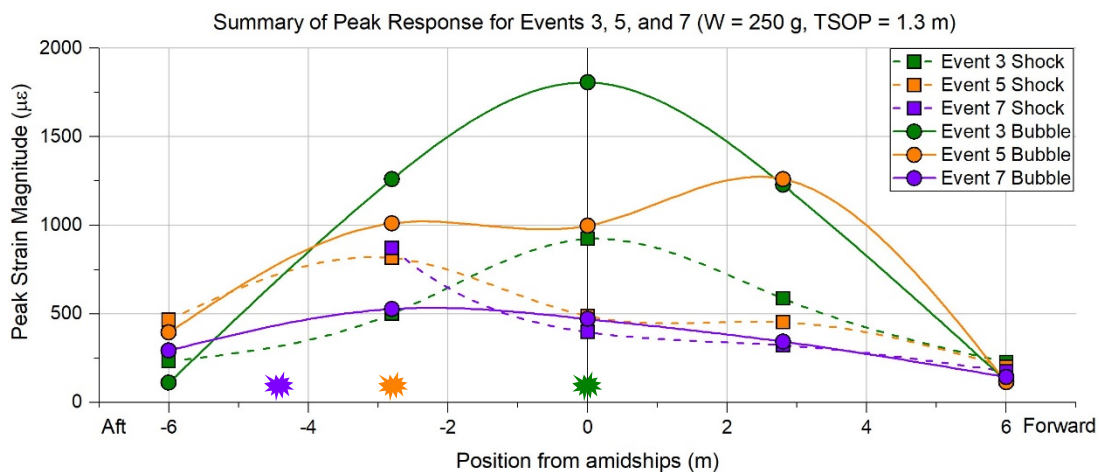


Figure 23: Summary of the peak strain response from shock and bubble loading at each measurement location for Events 3, 5, and 7 (250 g, 1.3 m TSOP).

The peak responses due to bubble loading were substantially different for each event. As previously discussed, Event 3 with an amidships charge LSOP, exhibited the most severe bubble response out of all the events conducted, with a peak strain magnitude response of  $1806 \mu\epsilon$  at the amidships measurement location.

The peak bubble response observed in Event 5, was one of the most noteworthy observations in this investigation. Here, the peak response from the bubble loading measured at  $1260 \mu\epsilon$ , occurred at the 2.8 m forward location on the platform, while a lower peak response of  $1011 \mu\epsilon$  was measured at -2.8 m aft, in line with the charge LSOP.

The unexpected response from Event 5 was further investigated through examination of the transient strain gauge records, on portside at amidships (S2), 2.8 m forward (S9), and aft (S17) in Figure 24a. The frequency response plot of these signals is shown in Figure 24b. The transient results in Figure 24a demonstrate an amplification of the bending response during the first bubble cycle, which is consistent with an UNDEX induced whipping response. Unlike the other 250 g events conducted at amidships, there were different

bending mode responses occurring between each of the measurement locations. The amidships location (S2) was dominated by only one frequency response, the previously observed BM1 at 6.7 Hz, while the forward and aft locations contained a combined response of two dominant frequencies, the BM1 response and a response at 20 Hz. The transient measurements also show that the 20 Hz response was inverted between the 2.8 m forward (S9) and aft (S17) and had similar amplitude in each location which indicates the 20 Hz was antisymmetric about the amidships location. The absence of the 20 Hz response at amidships also indicates there is a node for this response at this location. Based on this behaviour and the modal analysis from Table 1, the 20 Hz response was identified as the second bending mode (BM2) of the submerged platform.

The interaction of these two bending modes is the most likely cause of the peak response occurring at the forward end, despite the aft end charge LSOP. While the BM1 response was symmetric about amidships, the BM2 response was antisymmetric, so BM responses in the forward and aft ends of the platform were always in opposing constructive and destructive interference cycles. It is seen in Figure 24a that due to the phase of these response frequencies, the constructive interference of BM2 at the forward location coincided with the peak bending response of BM1 while under the direct loading of the bubble, which resulted in the maximum bubble response occurring at this location.

As with other 250 g events discussed in the previous section, the platform response begins to undergo damped free vibration after the second bubble pulse. During this time, the phase of the response at the 2.8 m forward and aft locations shifts slightly which results in the forward and aft responses having similar amplitudes, with the response at the 2.8 m forward location still being marginally higher. The phase shift after the direct bubble loading is a strong indication that the vessel response was predominantly driven by the bubble pulsation frequency and the bubble and platform responses were decoupled after the second bubble pulse.

This result of the overall peak response occurring away from the SOP has important implications for assessment and recovery response of a real platform. It highlights that it is possible for a scenario to occur where the most susceptible part of the vessel is not at the location where a direct hit occurs. In this investigation, only a change in the LSOP between Events 3 and 5 reduced the overall severity of the response in Event 5 by 30% but more importantly, relocated the most severe location away from the SOP. Furthermore it should be noted that the severity at the 2.8 m forward location was essentially the same for both events, i.e. while the overall severity reduced, the 2.8 m forward location saw the same severity between both events. To correctly identify similar vulnerable scenarios of a platform, the full response would need to be replicated and therefore the entire platform structure would need to be considered in the analysis method. A simplified compartment or symmetric model would not be sufficient to capture this response.

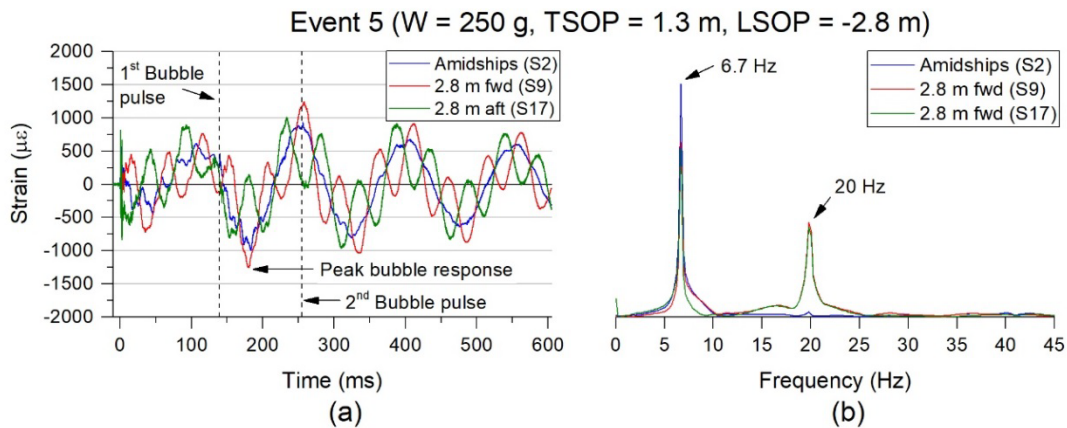


Figure 24: (a) Strain response from bubble loading at portside amidships (S2) and 2.8 m forward (S9) and aft (S17) from Event 5. (b) Frequency response plot of these records.

The peak response from bubble loading of the -4.3 m charge LSOP Event 7 was measured at only 528  $\mu\epsilon$ , as shown in Figure 25. This was a significant reduction of 71% compared to the amidships LSOP Event 3 shown in Figure 23. This was also the only 250 g event where the response due to bubble loading did not exceed the response from the direct shock loading. This reduction in response from the bubble loading is a remarkable result given the only difference in this event was the charge LSOP.

The reduced response from the bubble loading observed in Event 7 was further examined in the transient strain gauge records taken at the portside amidships (S2) and 2.8 m forward (S9) and aft (S17), presented in Figure 25a. Here it is apparent that after the shock wave, there is no amplification of the bending response until the first bubble pulse. In fact, between the shock wave and the first bubble pulse, the bending response amplitude decayed. The same was true for the bending responses that occurred between the first and second bubble pulses. This behaviour indicates that unlike all other 250 g events, the platform's response was not being driven by the under-pressure of the first bubble cycle. Only the direct pulse loads from the bubble's collapse were able to induce a notable response after the shock wave. Therefore, this event has demonstrated that by only adjusting the charge LSOP parameter, the bubble and platform responses became uncoupled. It is possible higher strains may have occurred at the SOP during the bubble loading, but no strain gauges were placed at this location. The lower responses measured at other locations along the platform length in summary of the peak strain response from shock and bubble loading at each measurement location for Events 3, 5, and 7 (250 g, 1.3 m TSOP) Figure 23, suggest that it is unlikely the strains would have been significantly larger at the SOP.

Unlike all other 250 g events, the amplitude of the response measured at the 2.8 m forward and aft locations from gauges S9 and S17 was not equivalent. For every second cycle of the bending response at these locations, the peaks at the aft end (S17) were on average 130  $\mu\epsilon$  larger than the forward end (S9) while under loading from the bubble. The frequency response plot from a FFT of the transient strain records, presented in Figure 25b, indicated that unlike all other 250 g events, the dominant bending response for Event 7 was the previously identified BM2 at a frequency of 20 Hz. Minor responses of the previously identified BM1 at 6.7 Hz and BM3 at 41 Hz were also present. The different amplitudes

seen at every second cycle of the 2.8 m forward and aft locations can be explained by the superimposed interaction of the dominant, antisymmetric BM2 and minor, symmetric BM3 responses. The BM3 response frequency is approximately double the BM2 response frequency, resulting in every second BM3 cycle being in phase with BM2. The combination of the periodic phase alignment and the different symmetry conditions of these responses about amidships resulted in constructive and deconstructive interference cycles consistently occurring at the aft and forward ends of the platform respectively.

The results for Event 7 demonstrate that if the SOP is aligned with a node response of the primary bending mode shape of a platform, the severity of the platform's response from bubble loading can be greatly reduced, to the point that the initial shock response is of a greater concern.

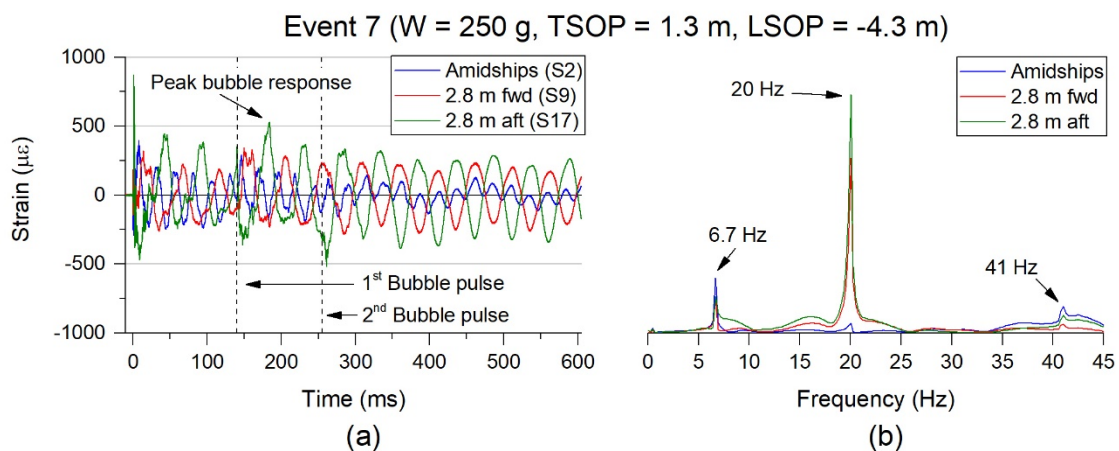


Figure 25: (a) Strain response from bubble loading at portside amidships (S2), 2.8 m forward (S9) and aft (S17) from Event 7. (b) Frequency response plot of these records.

The results for the smaller 43 g charge at 0.8 m TSOP (Events 4, 6, and 8) are now considered. The peak strain response magnitude from shock and bubble loads at each measurement location are summarised in Figure 26.

There was a noticeable disparity of the peak shock response between what should have been similar Event 4 and Events 6 and 8, shown in Figure 26. The peak response of Event 4 measured  $863 \mu\epsilon$ , compared with just under  $600 \mu\epsilon$  for Events 6 and 8. There are two explanations for why this was the case. First, the overall reduced energy of the 43 g explosive charge may have been insufficient to produce the same deflection of the platform when the LSOPs from Events 6 and 8 were closer to the ends, which contained a significant portion of the overall platform mass. Second, due to the interference that occurred at the stern measurement location, it is possible that the true maximum shock response for Events 6 and 8 was hidden within the distorted signal. While a set of results was able to be determined at the stern for Events 6 and 8, these may not be as reliable as other locations due to the interference issues. From these results, only the charge location of amidships LSOP Event 4 was able to produce the more significant global deflection of the platform.

Once again, only minor responses were measured at the bow and stern locations for both shock and bubble loading, with the largest response of  $360 \mu\epsilon$  measured at the stern in Event 6. Again, the peak responses at the stern were higher than at the bow, which can again be attributed to the closer proximity of the charge and the smaller perpendicular angles of incidence from the spherically spreading shock and bubble pulse waves.

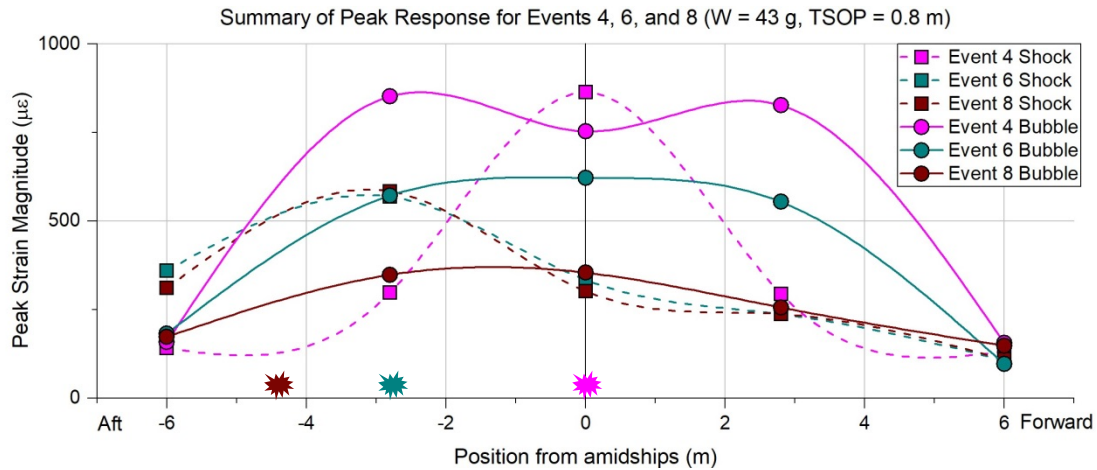


Figure 26: Summary of the peak strain response from shock and bubble loading at each measurement location for Events 4, 6, and 8 (43 g, 0.8 m TSOP)

The overall severity of the bubble response in these events decreased as the LSOP was moved away from amidships. The previously described amidships Event 4 had the most severe bubble loading response of the 43 g charge events, measuring  $852 \mu\epsilon$  at the -2.8 aft location.

The peak bubble response from the -2.8 m LSOP Event 6 was  $621 \mu\epsilon$ , measured at amidships, despite the LSOP offset. This peak response was 27 % lower than the amidships LSOP Event 4. This event did not have the same dip in the peak strain distribution along the hull length at amidships that was seen in Event 4, instead the severity at the amidships and 2.8 m forward and aft locations was very similar, with an average of  $582 \mu\epsilon$  and standard error of 3.5% between the peak measurements at these locations.

The cause of similar peak strain levels measured at the amidships, 2.8 m forward and aft locations for Event 6 is further examined in the transient strain gauge records from the portside gauges at amidships (S2), 2.8 m forward (S9), and aft (S17), presented in Figure 27a. It was found that in this transient response, the amidships strain levels were generally much lower than the forward and aft locations. The only exception to this was at the time of the first bubble pulse, where a large spike was observed in the amidships response. This spike was also the overall peak in the platform's response from the bubble loading for this event. It is also shown that the bending response between the shock wave and the first bubble pulse was amplified, indicating an UNDEX induced whipping response.

Between the first and second bubble pulses, the response was not symmetric between the forward and aft ends of the platform. This non-symmetric behaviour could be due to the bubble locally forcing the aft end and because the lower energy of the 43 g event was

insufficient to induce the same motion into the forward end. Additionally there was a difference between the bubble pulsation frequency of 12.9 Hz for the 43 g charge compared to any of the bending mode frequencies of the submerged platform, which means the pulsating bubble was unable to excite a distinct response in the platform. While the bubble was capable of initiating a whipping response, it was not able to maintain a driving force over the full platform length beyond the first bubble pulse, and the platform's inertia appears to have dominated the motion after the first bubble pulse. Beyond the second bubble pulse the platform started to undergo damped free vibration, where the amplitude of the responses at the 2.8 m forward and aft locations was nearly always double that of the amidships response amplitude.

The frequency response of the three locations is determined by applying a FFT on the transient signals to produce a frequency response plot in Figure 27b. Three frequencies were noted, all of which have previously been observed and identified in this investigation. This event was one of the few that exhibited an UNDEX induced whipping response which was not dominated by BM1 at 6.7 Hz. Instead, BM2 at 20 Hz is the dominant response, which is apparent in the previously noted larger responses occurring at the forward and aft locations of the transient records in Figure 27a. A minor contribution of BM3 at 41 Hz was also present in all three records. This can be clearly seen interacting with BM1 on the superimposed response measured at amidships during free-damped vibration in Figure 27a. The BM3 response did not appear to have any significant interference with the dominant BM2 response at the 2.8 m forward and aft locations.

Like Event 4, Event 6 has shown that when higher modal responses are excited by the UNDEX loads, there can be scenarios where there are multiple points of similar severity over the platform length. Event 6 also shows that this can be the case even when the UNDEX event occurs away from amidships and like Event 5, it highlights that the most severe response from bubble loading may not always occur at the SOP.

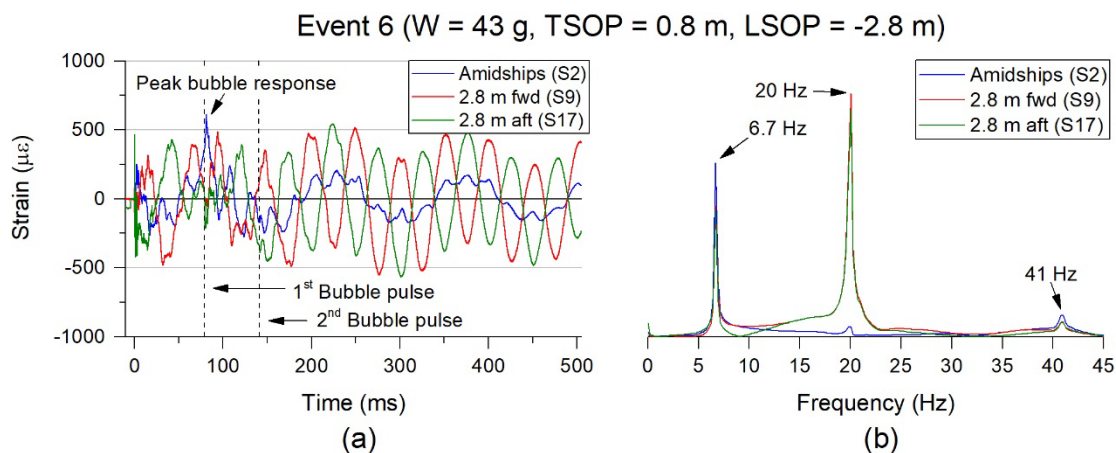


Figure 27: (a) Strain response from bubble loading at portside amidships (S2) and 2.8 m forward (S9) and aft (S17) from Event 6. (b) Frequency response plot of these records.

The peak bubble response from the -4.3 m LSOP Event 8 measured  $354 \mu\epsilon$ , a reduction of 58 % compared to the amidships LSOP Event 4. The bubble response in Event 8 was very similar to what was observed in Event 7 and while all other 43 g events had a similar

severity between the shock and bubble responses, Event 8's peak bubble response was much lower than its peak shock response.

The greatly reduced response from bubble loading was found to be due to the same reasons discussed for Event 7. The transient strain gauge records from amidships (S2) and 2.8 m forward (S9) and aft (S17), presented in Figure 28a, show that like Event 7, the initial bending response of the structure prior to the first bubble pulse did not amplify. This behaviour combined with the overall reduced strain levels during the bubble loading indicate that no significant whipping response was induced by the UNDEX loading. The peak responses due to bubble loading for this event are only due to the pressure pulse loading that was emitted during the first bubble cycle collapse. The different amplitudes between the forward and aft locations are also due to the symmetry conditions and phase alignment of BM2 and BM3 discussed for Event 7. The FFT frequency response results in Figure 28b, show that all previously identified frequency response components were present in this event, and also like Event 7, the dominant bending response for Event 8 was due to BM2 at 20 Hz.

Given the similarity of the Event 8 response results to those in Event 7, the same conclusions may be drawn and extended to apply to this smaller charge size. To reiterate, the results of both Events 7 and 8 have demonstrated that if the SOP was aligned with a node response of the primary bending mode of a platform, the severity of the platform's response from bubble loading was greatly reduced, to the point that the initial shock response was of a greater concern. As this has been observed for two different charge sizes and TSOP distances, it would appear this was a function of the LSOP in relation the platform's primary bending response shape. Because modal response shapes are fundamental physical attribute of any structure, it is suggested that any similar structure could be inherently "hardened" against a whipping response if the UNDEX SOP can be influenced to coincide with the node position of the structure's primary bending response.

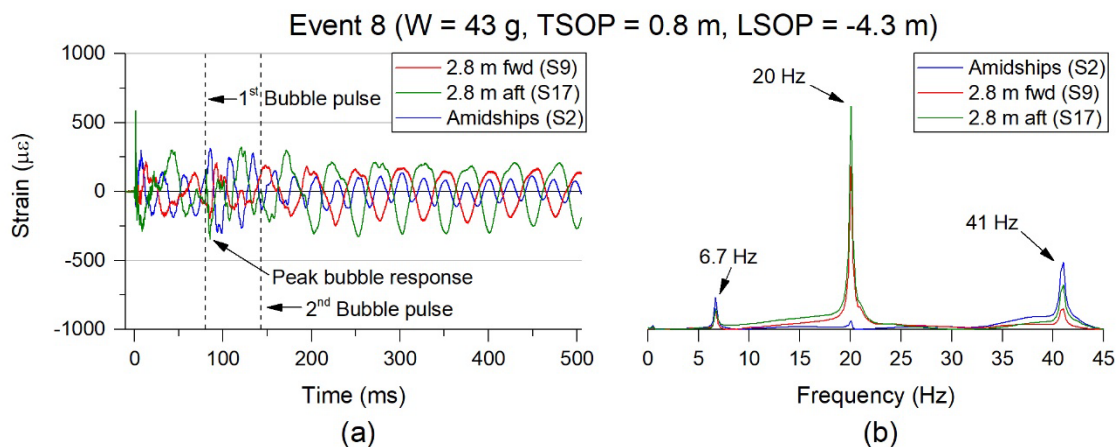


Figure 28: (a) Strain response from bubble loading at portside amidships (S2), 2.8 m forward (S9), and aft (S17) from Event 8. (b) Frequency response plot of these records.

The effect of LSOP on the peak strain response magnitude is summarised in Figure 29. Here it is clearly shown that with an  $R^2$  of -0.05, the LSOP variable had no correlation on the severity of the shock response for these events. For the bubble response, there was a weak linear trend with an  $R^2$  of 0.52, where the peak response reduced as the charge was

moved further from amidships (LSOP = 0). The spread between the bubble responses of different events at each LSOP also reduced, which indicates the other variables of charge size and TSOP had a diminishing effect on the peak strain response as LSOP moved further from amidships. While it was noted that the results for Event 7 may have been slightly larger due to the strain gauge locations, this would only result in a stronger correlation between the LSOP and peak platform response from bubble loading. Further data is required to quantitatively determine a relationship between the LSOP and the peak strain response on a submerged hollow cylindrical free-free ended beam.

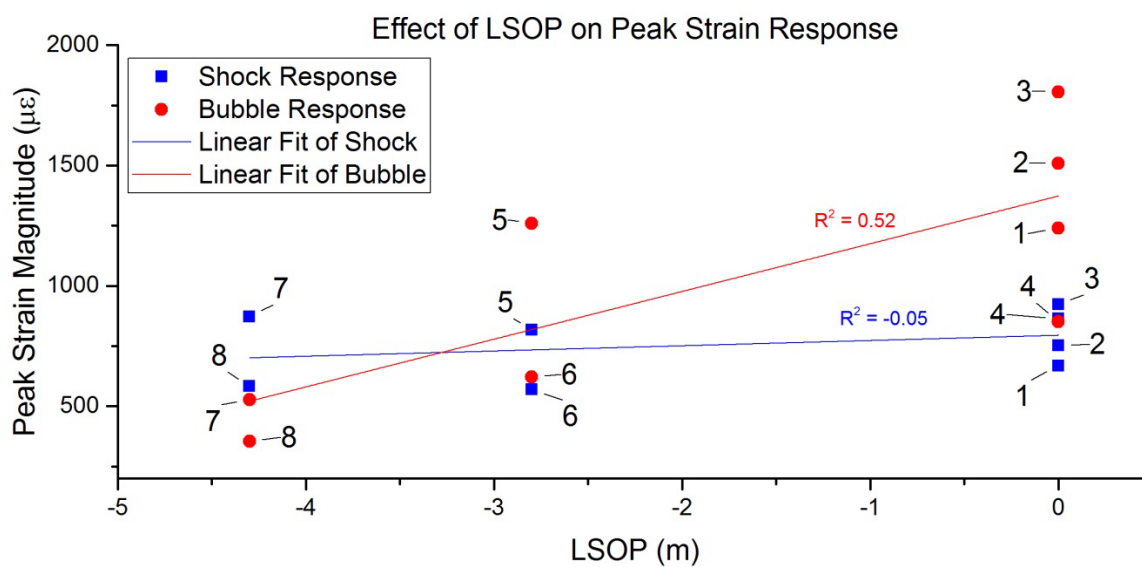


Figure 29: The effect of LSOP on the peak strain magnitude response for all events

A final comparison is made between the pressure impulse from Table 7 and the peak strain magnitude measurements of all events for shock and bubble responses in Figure 30, where the pressure impulse values for Events 7 and 8 are taken as an average of the similar 250 g Events 3 and 5, and 43 g Events 4 and 6 respectively. A linear fit was performed on the amidships Events 1 - 4, with a forced intercept at point (0, 0), which indicated a strong correlation between the peak strain and pressure impulse. The points from Event 4 fall outside the confidence band, which suggests this trend may only be valid for the 250 g charge, and further work would be required to determine if the trend is consistent across different charge sizes.

With the exception of Event 4, the shock responses of all similar events were closely clustered and there was a strong linear correlation of increasing shock response from larger pressure impulses. The clustering further indicates that the LSOP had essentially no effect on the severity of the shock response. The linear trend is shown to extend to the amidships bubble responses from Events 1 - 4. It is also shown that the bubble response away from amidships were lower than their amidships counterparts. There is an apparent linear trend between events with the same LSOP, where the LSOP reduces the gradient of the linear bubble response trend, compared to amidships. However there is insufficient data to quantitatively confirm this.

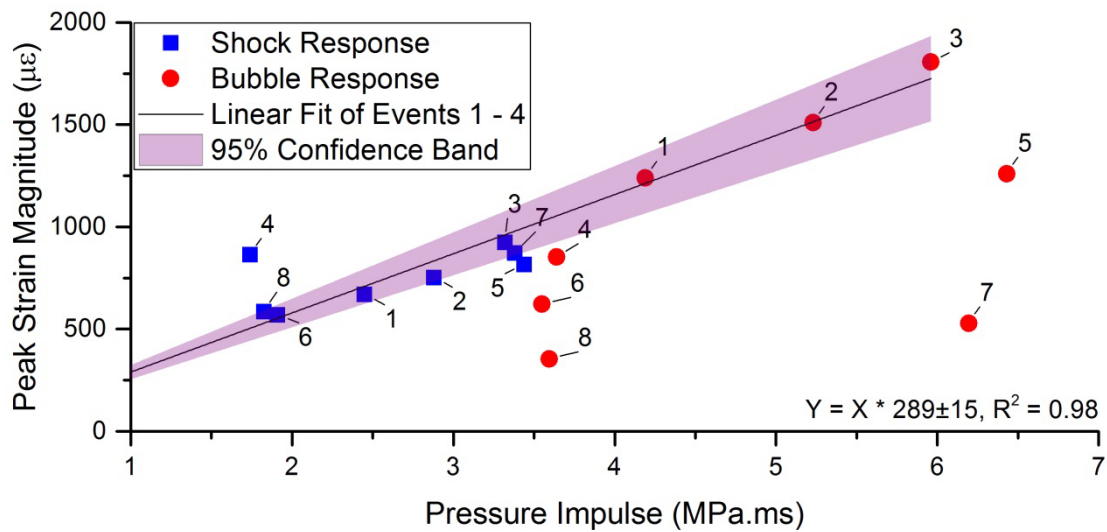


Figure 30: Peak strain magnitudes from shock and bubble response compared to the respective pressure impulses of all events

## 4 Conclusion

A set of eight underwater explosion experiments were conducted to investigate the whipping response of a submerged 12 m long, 0.4 m diameter cylindrical platform. Two Pentolite charge sizes (250 g and 43 g) at stand-off distances from 1.8 m to 0.8 m, and at different longitudinal positions along the hull length were used in this experiment. All UNDEX events were conducted with the charge and the platform at a depth of 5 m.

Measured incident pressures showed good correlation with theory for the first bubble cycle. However, current similitude equations under-predicted the second bubble period and new  $K$  coefficients were identified and presented from this experimental dataset. Through integration of the incident pressure-time data, it was found for both charge sizes that 35.1% and 64.9% of the total pressure impulse was associated with the shock wave and bubble respectively.

The severity of whipping induced bending responses was found to depend on the magnitude and relative phasing contributions from the first three global bending modes of the submerged platform. For a given charge size and stand-off distance, the contribution of a mode increased with the proximity of the bubble frequency to the modal frequency, and with the physical proximity of the longitudinal position of the charge and the peak deflection of the mode shape. This was predominantly influenced by the first bending mode shape, where charges detonated at amidships produced the most severe whipping responses from bubble loads, while charges detonated near the node of the first bending mode shape did not exhibit a significant whipping response from the bubble loads. The interaction of the dominant mode shapes also caused the peak bending response of some events to occur at locations away from the charge stand-off point.

It is suggested that if the stand-off location along the platform length can be influenced to occur at the node of the primary bending mode shape, the platform will be inherently hardened against a severe whipping response. Additionally, should a scenario occur where multiple bending modes are excited, locations away from the stand-off point may need to be assessed, and these may undergo a more severe response than at the stand-off point.

Further research is required to understand and determine the limits of how the relative size of a bubble to a structure will affect the degree of coupled bubble-structure interaction, and if there is an optimal ratio for maintaining a coupled response. Additional investigation is required to understand the effects that the 43 g charge and other charge sizes at additional stand-off distances have on the whipping response.

## 5 Acknowledgements

This work was conducted with support from an Australian Government Research Training Program scholarship and the ARC Research Training Centre for Naval Design and Manufacturing (RTC-NDM). The RTC-NDM is a University-Industry partnership established under the Australian Research Council Industry Transformation grant scheme (ARC IC140100003), to train the next generation of Naval Manufacturing and Design personnel and provide the naval manufacturing industry with supporting research.

The authors also wish to acknowledge the Defence Science and Technology Group, particularly the members of the Dynamic Military Loads STC, for the extensive technical advice and experimental support while using their UNDEX testing and data processing facilities to undertake this investigation. A special mention to Craig Flockhart and Andrew Krelle for their assistance with the design, and processing and interpretation of the experiment and results.

## 6 References

1. Cole, R. H. (1948) *Underwater Explosions*. Princeton, New Jersey, Princeton University Press
2. Dobratz, B. (1981) *LLNL explosives handbook: properties of chemical explosives and explosives and explosive simulants*. Lawrence Livermore National Lab., CA (USA)
3. Reid, W. D. (1996) *The Response of Surface Ships to Underwater Explosions*. DSTO-GD-0109, Melbourne, Victoria, Defence Science and Technology Organisation
4. Swisdak, M. M. (1978) *Explosion Effects and Properties. Part II. Explosion Effects in Water*. Silver Spring, MD, USA, Naval Surface Weapons Center
5. Swift, E. and Decius, J. C. (1947) Measurement of Bubble Pulse Phenomena, III: Radius and Period Studies. In: *Underwater Explosion Research*. Vol. 2. Washington D.C., 1950, Office of Navy Research
6. Barker, D. (2010) The Case for Impulse - Analysis of Conventional Structures Subjected to Blast Loads. In: *34th Department of Defence Explosives Safety Board*

- Seminar, Portland, Oregon: 13-15 July 2010, ABSG CONSULTING INC SAN ANTONIO TX
7. Cooker, M. J. and Peregrine, D. (1995) Pressure-impulse theory for liquid impact problems. *Journal of Fluid Mechanics* **297** 193-214
  8. Blake, F. G. (1949) Bjerknes Forces in Stationary Sound Fields. *The Journal of the Acoustical Society of America* **21** (5) 1949/09/01 551-551
  9. Birkhoff, G. and Zarantonello, E. H. (1957) *Jets, Wakes, and Cavities*. Applied Mathematics and Mechanics, Garrett, B. and E.H, Z. ed. Vol. Volume 2, Elsevier
  10. Chisum, J. E. and Shin, Y. S. (1997) Explosion Gas Bubbles Near Simple Boundaries. *Shock and Vibration* **4** (1)
  11. Tomita, Y., Robinson, P. B., Tong, R. P., Blake, J. R. (2002) Growth and collapse of cavitation bubbles near a curved rigid boundary. *Journal of Fluid Mechanics* **466** 259-283
  12. Brett, J. M. and Yiannakopoulos, G. (2008) A study of explosive effects in close proximity to a submerged cylinder. *International Journal of Impact Engineering* **35** (4) 4/ / 206-225
  13. Hung, C. F. and Hwangfu, J. J. (2010) Experimental study of the behaviour of mini-charge underwater explosion bubbles near different boundaries. *Journal of Fluid Mechanics* **651** 55-80
  14. Zhang, A. M., Wang, S. P., Huang, C., Wang, B. (2013) Influences of initial and boundary conditions on underwater explosion bubble dynamics. *European Journal of Mechanics - B/Fluids* **42** 11/ / 69-91
  15. Wang, Q. X., Yeo, K. S., Khoo, B. C., Lam, K. Y. (1996) Nonlinear interaction between gas bubble and free surface. *Computers & Fluids* **25** (7) 1996/09/01/ 607-628
  16. Pearson, A., Cox, E., Blake, J. R., Otto, S. R. (2004) Bubble interactions near a free surface. *Engineering Analysis with Boundary Elements* **28** (4) 2004/04/01/ 295-313
  17. Brujan, E. A., Nahen, K., Schmidt, P., Vogel, A. (2001) Dynamics of laser-induced cavitation bubbles near elastic boundaries: influence of the elastic modulus. *Journal of Fluid Mechanics* **433** 283-314
  18. Brujan, E. A., Nahen, K., Schmidt, P., Vogel, A. (2001) Dynamics of laser-induced cavitation bubbles near an elastic boundary. *Journal of Fluid Mechanics* **433** 251-281
  19. Brujan, E. A., Keen, G. S., Vogel, A., Blake, J. R. (2002) The final stage of the collapse of a cavitation bubble close to a rigid boundary. *Physics of Fluids (1994-present)* **14** (1) 85-92
  20. Cui, P. Z., A. M.; Wang, S. P. (2016) Small-charge underwater explosion bubble experiments under various boundary conditions. *Physics of Fluids* **28** (11) 2016/11/01 117103
  21. Hicks, A. N. (1972) *The theory of explosion induced ship whipping motions*. St Leonard's Hill, Dunfermline, U.K., Naval Construction Research Establishment
  22. Hunter, K. S. and Geers, T. L. (2004) Pressure and velocity fields produced by an underwater explosion. *The Journal of the Acoustical Society of America* **115** (4) 1483-1496
  23. Geers, T. L. and Hunter, K. S. (2002) An integrated wave-effects model for an underwater explosion bubble. *Journal of the Acoustical Society of America* **111** (4) 1584-1601

24. Gibson, D. C. and Blake, J. R. (1980) *7th Australasian Conference on Hydraulics and Fluid Mechanics 1980: Preprints of Papers*, Institution of Engineers, Australia
25. Blake, J., Taib, B. and Doherty, G. (1986) Transient cavities near boundaries. Part 1. Rigid boundary. *Journal of Fluid Mechanics* **170** 479-497
26. Blake, J., Hooton, M., Robinson, P., Tong, R. (1997) Collapsing cavities, toroidal bubbles and jet impact. *Philosophical Transactions of the Royal Society of London A: Mathematical, Physical and Engineering Sciences* **355** (1724) 537-550
27. Keil, A. H. (1961) *The response of ships to underwater explosions*. Washington D.C., David Taylor Model Basin
28. Benjamin, T. B. and Ellis, A. T. (1966) The Collapse of Cavitation Bubbles and the Pressures thereby Produced against Solid Boundaries. *Philosophical Transactions of the Royal Society of London. Series A, Mathematical and Physical Sciences* **260** (1110) 221-240
29. Lauterborn, W. and Bolle, H. (1975) Experimental investigations of cavitation-bubble collapse in the neighbourhood of a solid boundary. *Journal of Fluid Mechanics* **72** (02) 391-399
30. Plesset, M. S. and Chapman, R. B. (1971) Collapse of an initially spherical vapour cavity in the neighbourhood of a solid boundary. *Journal of Fluid Mechanics* **47** (02) 283-290
31. Zhang, S., Wang, S. P. and Zhang, A. M. (2016) Experimental study on the interaction between bubble and free surface using a high-voltage spark generator. *Physics of Fluids* **28** (3) 032109
32. Shurcliff, W. A. (1947) *Bombs at Bikini: The Official Report of Operation Crossroads*. United States Joint Task Force One
33. Blevins, R. D. (1980) Formulas for natural frequency and mode shape. *Journal of Applied Mechanics* **47** 461
34. Burcher, R. and Rydill, L. J. (1995) *Concepts in submarine design*. Vol. 2, Cambridge University Press
35. Bishop, J. H. (1993) Underwater shock standards and tests for naval vessels.
36. Welch, W. P. (1946) *Mechanical shock on naval vessels*, US Government Printing Office
37. Hellqvist, K. (1981) A large-scale submarine shock test carried out as part of the Swedish Shock Design Development Program. In: *The Shock and Vibration Bulletin*. Vol. 2. Naval Research Laboratory, Washington D.C., Shock and Vibration Information Center 129-136
38. De Candia, S., Ojeda, R., Reid, W. D., Ratcliffe, M., Binns, J. (2017) The Whipping Response of a Submerged Free-Free Cylinder Due to Underwater Explosions. In: *International Maritime Conference - Pacific 2017*, Sydney
39. Chertock, G. (1953) The Flexural Response of a Submerged Solid to a Pulsating Gas Bubble. *Journal of Applied Physics* **24** (2) 02// 192
40. Chertock, G. (1970) Transient Flexural Vibrations of Ship-Like Structures Exposed to Underwater Explosions. *The Journal of the Acoustical Society of America* **48** (1B) 170-180
41. Bannister, K. A. (1980) Whipping analysis techniques for ships and submarines. *The Shock and Vibration Bulletin* **50** 83
42. Lewis, F. M. (1929) The inertia of the water surrounding a vibrating ship. *Trans. SNAME* **37** 1-20

43. DeRuntz, J. A. (1989) *Proceedings of the 60th Shock and Vibration Symposium*. Vol. 1, Virginia Beach, Virginia, Shock and Vibration Information Center
44. Geers, T. L. (1978) Doubly asymptotic approximations for transient motions of submerged structures. *The Journal of the Acoustical Society of America* **64** (5) 1500-1508
45. Zong, Z., Wang, J., Zhou, L., Zhang, G. (2015) Fully nonlinear 3D interaction of bubble dynamics and a submerged or floating structure. *Applied Ocean Research* **53** 10// 236-249
46. Zhang, A. M., Yao, X. L. and Li, J. (2008) The interaction of an underwater explosion bubble and an elastic-plastic structure. *Applied Ocean Research* **30** (3) 7// 159-171
47. AS/NZS 1163:2009 (2009) AS/NZS 1163:2009 : *Cold-formed structural steel hollow sections*. Global, S.
48. AS 2129-2000 (R2016) (2000) AS 2129-2000 (R2016) : *Flanges for pipes, valves and fittings*. Global, S.
49. LSTC (2015) *LS-DYNA R8.0 Keyword Manual*. Livermore, CA, Livermore Software Technology Corporation
50. LSTC (2014) *USA LS-DYNA Users Manual - USA Release 7.5*. Livermore, CA, Livermore Software Technology Corporation
51. Deruntz, J. A. and Geers, T. L. (1978) Added mass computation by the boundary integral method. *International Journal for Numerical Methods in Engineering* **12** (3) 531-550
52. Elsys AG (2012) *TPCX & TPCE Specification*. Mellingerstrasse 12, CH-5443 Niederrohrdorf, Switzerland, Elsys AG
53. PCB Piezotronics (2015) *Model W138A05 ICP Pressure Sensor Installation and Operating Manual*. 3425 Walden Avenue, Depew, NY 14043, PCB Piezotronics, Inc.
54. Neptune Sonar Limited (2017) *Shock Gauge Transducer Datasheet - Model T11*. Kelk Lake, Kelk, East Yorkshire, Neptune Sonar Limited
55. Micro Measurements (2014) *Special Use Sensors - Weldable Strain Gages*. Malvern, Pennsylvania, United States, Vishay Precision Group, Inc.
56. TML (2017) *High temperature Weldable Strain Gauges Series AW. 8-2*, Minami-Ohi 6-chome, Shinagawa-ku, Tokyo 140-8560, Japan, Tokyo Sokki Kenkyujo Co., Ltd.
57. Walter, P. L. (2001) *The handbook of dynamic force, pressure and acceleration measurement*. San Juan Capistrano, CA, USA. Meggitt, Endevco.
58. PCB Piezotronics (2017) *Model 350B21 Accelerometer Installation and Operating Manual*. 3425 Walden Avenue, Depew, NY 14043, PCB Piezotronics, Inc.
59. PCB Piezotronics (2012) *Model 350B24 Shear ICP Shock Accelerometer Installation and Operating Manual*. 3425 Walden Avenue, Depew, NY 14043, PCB Piezotronics, Inc.
60. PCB Piezotronics (2017) *Model 3501A2020KG High Amplitude MEMS Shock Accelerometer Installation and Operating Manual*. 3425 Walden Avenue, Depew, NY 14043, PCB Piezotronics, Inc.
61. PCB Piezotronics (2017) *Model 3501A2060KG High Amplitude MEMS Shock Accelerometer Installation and Operating Manual*. 3425 Walden Avenue, Depew, NY 14043, PCB Piezotronics, Inc.
62. PCB Piezotronics (2011) *Model 3503A1020KG/ACS-62BT Triaxial High Amplitude MEMS Shock Accelerometer Installation and Operating Manual*. 3425 Walden Avenue, Depew, NY 14043, PCB Piezotronics, Inc.

63. Meggitt Sensing Systems (2017) *Endevco Piezoresistive Accelerometer Model 7270A*. 14600 Myford Road Irvine CA, Meggitt Sensing Systems
64. Scavuzzo, R. J. and Pusey, H. C. (2011) *Principles and techniques of shock data analysis*, Shock and Vibration Information Analysis Center
65. Pacific Instruments (2017) *Series 5800 Conditioning & Transient Recording Systems*. 4080 Pike Lane, Concord, CA., Pacific Instruments

## Appendix A Additional measurement systems

Additional measurement transducers were installed in the platform to measure acceleration and velocity responses. The results of these transducers were not considered in the present investigation. A large number of different accelerometer models were used to compare the responses between different models and designs, and for redundancy. Two UERD Velocity meters were installed at each measurement station to directly measure the velocity response in vertical and athwartships directions, and compare against the integrated results from accelerometer transducers. The transducer models, quantity and designation are listed in Table 8.

Table 8: Pressure and strain measurement transducer details

Transducer	Quantity	Designation	Ref.
<b>Acceleration</b>			
PCB 350B01	5	A1, 3, 5, 7, 9	[58]
PCB 350B21	2	A6, 8	[58]
PCB 350C02	4	A12-13, 18-19, 21-22	[59]
PCB 350B24	6	A14-16	[59]
PCB 350B50 Triaxial	1	A27-29	[60]
PCB 3501A2060KG	3	A2, 4, 10	[61]
PCB 3501A2020KG	3	A17, 20	[60]
PCB 3503A1020KG Triaxial	1	A24-26	[62]
Endevco 7270A-200K	1	A23	[63]
Endevco 7270A-6K	1	A11	[63]
<b>Velocity</b>			
UERD Velocity meter	10	V1-10	[64]

Pacific Instruments 5871 data acquisition systems [65] were used to sample accelerometers. While all velocity meters were sampled through the Elsys TraNET data acquisition system [52]. Both of these systems were located on shore as shown in Figure 4. All accelerometers and velocity meters were screw mounted on  $140 \times 140 \times 20$  mm aluminium blocks, machined to the round hull profile and attached by epoxy adhesive. The gauges were located along the hull as described by the polar coordinate system in Figure 31, with the coordinates of each transducer listed in Table 9.

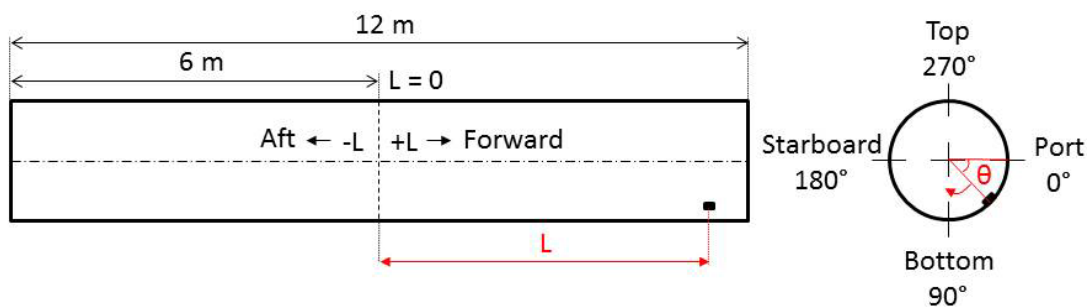


Figure 31: Internal arrangement of additional measurement transducers

Table 9: Accelerometer and velocity meter details and polar coordinates (continues on next page)

Station	Gauge	L (mm)	$\theta^\circ$	Orientation
1 Bow	V6	5930	0	Horizontal
	V10	5835	90	Vertical
	A14	5873	356	Horizontal
	A15	5873	4	Horizontal
	A16	5892	90	Vertical
	A27	5873	4	Longitudinal
	A28	5873	4	Vertical
	A29	5873	4	Horizontal
2 2.8 m Fwd	V4	2850	0	Horizontal
	V8	2750	90	Vertical
	A11	2907	356	Horizontal
	A12	2907	4	Horizontal
	A13	2807	86	Vertical

Table 9 continued

Station	Gauge	L (mm)	$\theta^\circ$	Orientation
3 Amidships	V1	-50	0	Horizontal
	V2	50	90	Vertical
	A1	7	356	Horizontal
	A2	7	4	Horizontal
	A3	50	352	Horizontal
	A4	50	0	Horizontal
	A5	-107	356	Horizontal
	A6	-107	4	Horizontal
	A7	-75	352	Horizontal
	A8	-25	352	Horizontal
	A9	107	86	Vertical
	A10	107	94	Vertical
	A23	50	4	Horizontal
	A24	-300	180	Longitudinal
	A25	-300	180	Vertical
	A26	-300	180	Horizontal
4 -2.8 m Aft	V3	-2850	0	Horizontal
	V7	-2750	90	Vertical
	A17	-2907	356	Horizontal
	A18	-2907	4	Horizontal
	A19	-2807	86	Vertical
5 Stern	V5	-5930	0	Horizontal
	V9	-5835	90	Vertical
	A20	-5873	356	Horizontal
	A21	-5873	4	Horizontal
	A22	-5778	86	Vertical

## UNCLASSIFIED

<b>DEFENCE SCIENCE AND TECHNOLOGY GROUP DOCUMENT CONTROL DATA</b>		1. DLM/CAVEAT (OF DOCUMENT)	
2. TITLE The Whipping Response of a Submerged Platform Subjected to Near-field, Non-Contact Underwater Explosions		3. SECURITY CLASSIFICATION (FOR UNCLASSIFIED LIMITED RELEASE USE (U/L) NEXT TO DOCUMENT CLASSIFICATION)  Document (U) Title (U) Abstract (U)	
4. AUTHOR(S) Steven De Candia, Roberto Ojeda, Warren Reid and Max Ratcliffe		5. CORPORATE AUTHOR Defence Science and Technology Group 506 Lorimer Street Fishermans Bend VIC 3207	
6a. DST GROUP NUMBER DST-Group-RR-0451	6b. AR NUMBER AR-017-282	6c. TYPE OF REPORT Research Report	7. DOCUMENT DATE September 2018
8. TASK NUMBER 07/386	9. TASK SPONSOR Future Submarine Project	10. RESEARCH DIVISION Maritime Division	
11. MSTC Maritime Platform Performance		12. STC Dynamic Military Loads	
13. SECONDARY RELEASE STATEMENT OF THIS DOCUMENT  <i>Approved for public release.</i>  OVERSEAS ENQUIRIES OUTSIDE STATED LIMITATIONS SHOULD BE REFERRED THROUGH DOCUMENT EXCHANGE, PO BOX 1500, EDINBURGH, SA 5111			
14. DELIBERATE ANNOUNCEMENT Australian Department of Defence and Defence Force Personnel.			
15. CITATION IN OTHER DOCUMENTS Yes			
16. RESEARCH LIBRARY THESAURUS Underwater explosions, Structural response, Experimental analysis, Bubbles, Shock			
17. ABSTRACT  An experimental investigation of an underwater explosion (UNDEX) induced whipping response was conducted on a submerged platform. The platform was subjected to eight near-field, non-contact UNDEX events, using two explosive charge sizes at three longitudinal positions along the hull length, coinciding with predetermined peak and node positions of the natural bending mode responses of the platform. We found that stand-off positions at amidships, coinciding with the peak response of the first bending mode, produced the most severe whipping response. Stand-off positions located at the node of the first bending mode had a greatly reduced whipping response for the same charge size and transverse stand-off distance. Stand-off positions away from amidships demonstrated multiple bending mode responses, which for the larger charge size resulted in the peak response occurring away from the initial stand-off position. These results have an implication on how navy platform assessments are undertaken, and suggests that whipping responses require more detailed consideration to understand a platform's limitations against an UNDEX event.			

UNCLASSIFIED